Journal of Medicinal Chemistry

pubs.acs.org/jmc

Article

In Situ NADH-Activated BODIPY-Based Macrocyclic Supramolecular Photosensitizer for Chemo-Photodynamic Synergistic Tumor Therapy

Zhuo Lei, Ya-Hui Song, Yuan-Li Leng, Yi-Jun Gu, Miao Yu, Yong Chen, Qilin Yu, and Yu Liu*

Cite This: https://doi.org/10.1021/acs.jmedchem.5c00094

Read Online

ACCESS | Metrics & More | Article Recommendations | Supporting Information

ABSTRACT: Photodynamic therapy (PDT) based on supramolecular assembly has been receiving wide attention due to its great potential application in clinical treatment. Herein, we report a supramolecular photoelectron "reservoir" (SPR) constructed by tetracationic boron dipyrromethene (BODIPY)-based macrocycle (**BBox·**4Cl), doxorubicin (Dox), and tumor-targeted β-cyclodextrin-grafted hyaluronic acid (HACD). Upon irradiation, **BBox·**4Cl can in situ catalyze nicotinamide adenine dinucleotide (NADH) to continuously generate electrons to inject into SPR, which further transfers electrons to oxygen, inducing highly efficient hydroxyl radical generation even under hypoxia. Synergistically, Dox in SPR as "pump" can be encapsulated by **BBox·**4Cl and transport photoelectrons between two BODIPY units, while HACD as "sponge" can enrich **BBox·**4Cl by the electrostatic interaction to concentrate them closer in space, which facilitates intramolecular and intermolecular photoelectron transfer, respectively, and significantly enhances the generation of hydroxyl radicals. Meanwhile, electron replenishment in SPR causes NADH depletion and redox dysfunction, thereby accelerating the apoptosis and achieving highly effective synergistic tumor therapy.

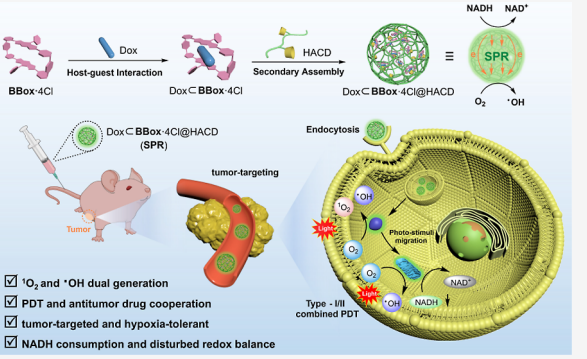

INTRODUCTION

Multivalent supramolecular assembly based on macrocycles such as cyclodextrin,[1−4] cucurbituril,[5−7] calixarene,[8,9] and pillararene,[10,11] has aroused wide attention, and many efforts have contributed to drug delivery,[12−16] controllable release,[17−19] bioimaging,[20−23] photodynamic therapy (PDT),[24−26] as well as numerous synergistic therapies[27−30] for diagnosis and treatment. Among them, macrocycle confined supramolecular assembly has emerged as a controllable modulation of photosensitizers to achieve precise and long-lasting PDT.[31] The capsulation of photosensitizers within macrocycles was found to not only improve the generation efficiency of reactive oxygen species (ROS) by increasing cellular uptake of drugs as well as regulating the intersystem crossing behavior of photosensitizers but also isolate the toxic components, reducing the side effects in PDT.[32−34] For example, Ikeda et al. found that the capsulation of aniline- or phenol-substituted porphyrins with trimethyl-β-cyclodextrin could significantly improve the photodynamic activity due to the efficient intracellular uptake.[35] Zhang et al. reported that cucurbit[7]uril could prolong the lifetime of the boron dipyrromethene (BODIPY)-based photosensitizer by host−guest interaction, which facilitated the energy transfer or electron transfer from photosensitizer to oxygen and improved ROS generation efficiency. Meanwhile, the obtained supramolecular photosensitizer avoided possible side effects due to photoinduced degradation after treatment.[36] Our group reported a polypeptide-involved supramolecular photodynamic system, which was constructed by host−guest interaction between cell-penetrating polypeptide-modified porphyrin and antimitotic polypeptide-modified permethyl β-cyclodextrin, respectively, could effectively achieve tubulin aggregates and improve the efficiency of singlet oxygen molecule ($^1O_2$) generation for PDT.[37] Recently, macrocycle-confined supramolecular assembly has also been found to be an effective strategy for the construction of type-I photosensitizers due to the electron transport facilitated by multivalent interaction.[38,39] In contrast to the ROS generated from most of the photosensitization system that underwent type-II PDT process and were represented by $^1O_2$ involving triplet to singlet energy transfer, the generation of hydroxyl radicals ($^{\bullet}OH$) or superoxide radical anions ($O_2^{\bullet-}$) with less oxygen dependence by the process of type-I PDT was able to overcome the unsatisfactory outcomes from hypoxia in PDT.[40−42] In this regard, Yang et al. reported a host−guest complex constructed

Received: January 11, 2025
Revised: February 13, 2025
Accepted: February 19, 2025

Scheme 1. Schematic Illustration of the NADH-Activated Supramolecular Photoelectron "Reservoir" (SPR) for Chemo-Photodynamic Synergistic Tumor Therapy.[a]

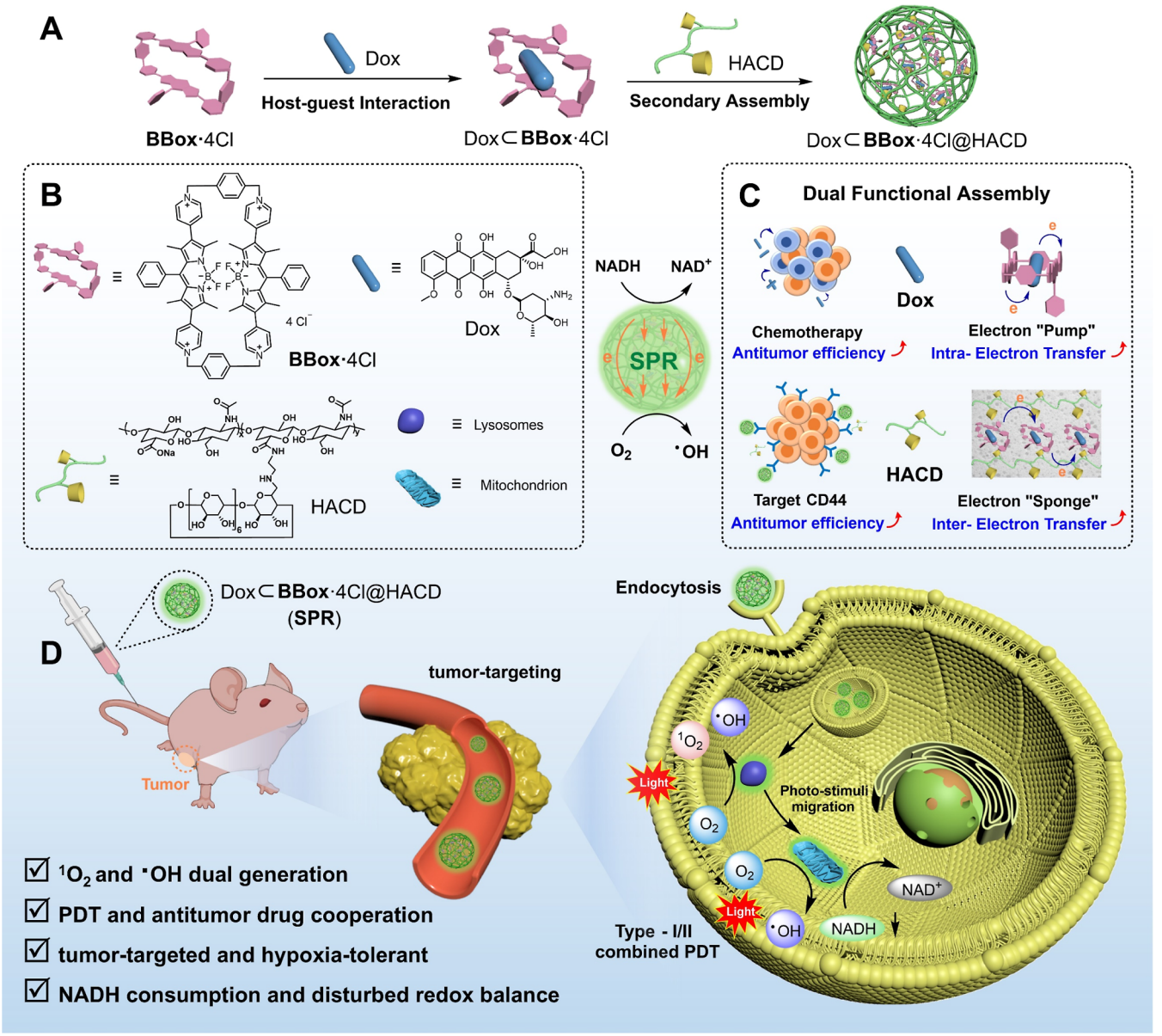

[a](A) Ternary spherical nanoparticles Dox ⊂ **BBox**·4Cl@HACD as SPR was constructed by **BBox**·4Cl, Dox, and HACD. (B) The chemical formula of **BBox**·4Cl, Dox, and HACD. (C) Antitumor drug Dox and tumor-targeted HACD in SPR was employed as "pump" and "sponge" for effective photoelectron transfer. (D) Dox ⊂ **BBox**·4Cl@HACD as SPR was applied for synergistic tumor therapy in vivo.

by an electron-rich pillar[5]arene and an electron-deficient iodide BODIPY, which could shorten the intermolecular distance between donor and acceptor sites, effectively converting type-II to type-I PDT for hypoxic tumor tissues.[38] As can be seen from the above research, although macrocycle binding photosensitizers have achieved many contributions in the PDT, NADH in situ tumor continuously produces electrons by photo-oxidation to pump into the photosensitized macrocyclic supramolecular assembly and then transports electrons to generate $^{\bullet}OH$ for type-I PDT, which is rarely reported to the best of our knowledge.

Herein, we report that a novel tetracationic macrocycle possessing a BODIPY skeleton encapsulates doxorubicin (Dox) as an antitumor drug to form the host−guest complex (Dox ⊂ **BBox**·4Cl) and further secondary assembles with tumor-targeted β-cyclodextrin grafted-hyaluronic acid (HACD) into spherical nanoparticles (Dox ⊂ **BBox**·4Cl@HACD) as supramolecular photoelectron "reservoir" (SPR), which can continuously grasp electrons from nicotinamide adenine dinucleotide (NADH) by catalytic oxidation and transfers them to oxygen, thus effectively generating $^{\bullet}OH$ for type-I/II combined synergistic tumor therapy (Scheme 1). The selective binding of Dox into the cavity of **BBox**·4Cl is favorable with a high binding constant of up to 8.05×10^5 M^{-1}, while the ternary supramolecular assembly Dox ⊂ **BBox**·4Cl@HACD not only can produce $^1O_2$ with a high quantum yield of 185%, but more intriguingly, as SPR generates $^{\bullet}OH$ by transferring electrons from NADH to oxygen. In particular, Dox in SPR acts as a "pump" to transport the electrons between two BODIPY units, leading to a favorable

https://doi.org/10.1021/acs.jmedchem.5c00094
J. Med. Chem. XXXX, XXX, XXX−XXX

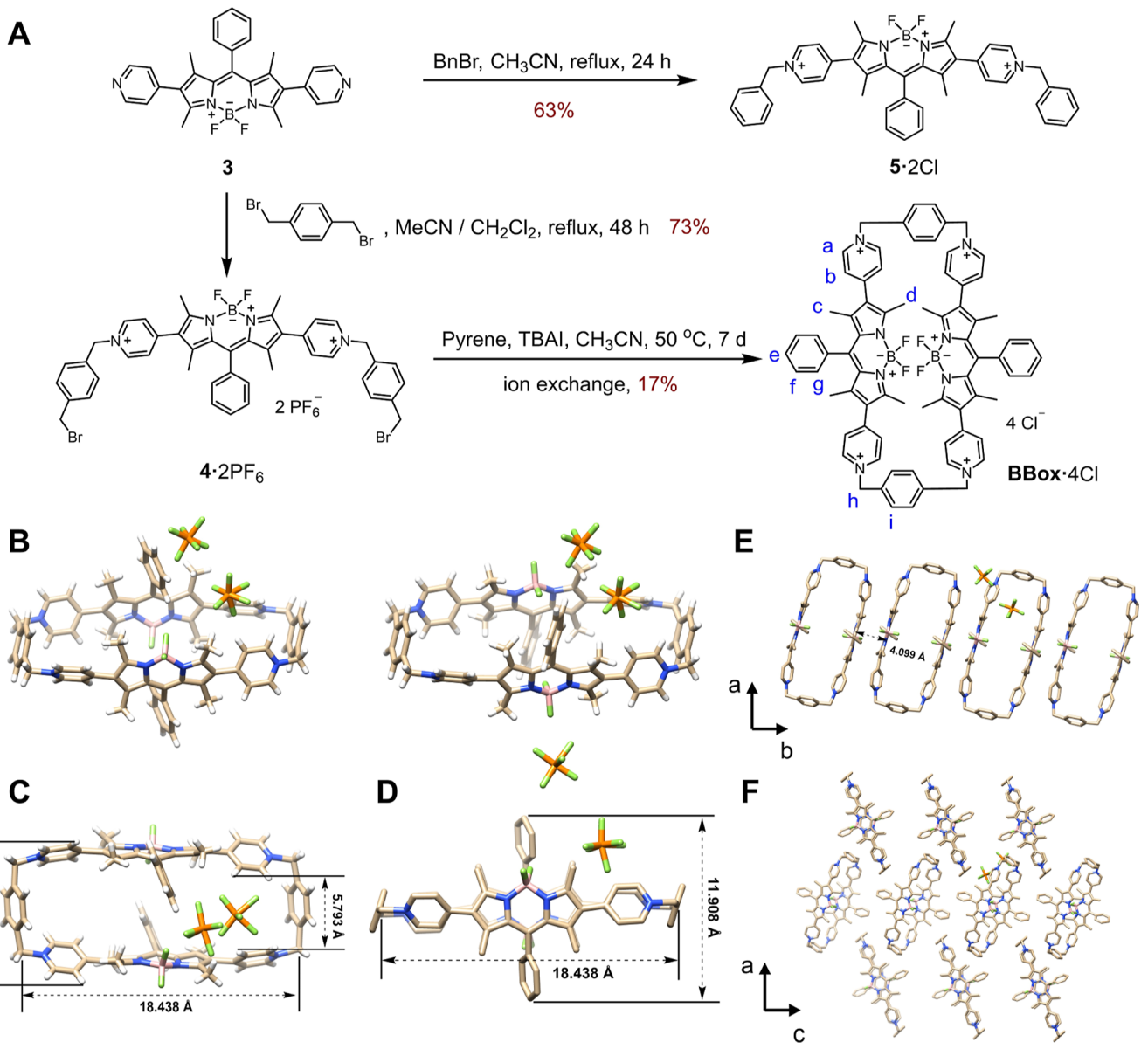

Figure 1. Synthesis and X-ray structure of **BBox**$^{4+}$ (CCDC: 2367093). (A) Synthesis route of reference compound **5**·2Cl and BODIPY-based molecular macrocycle **BBox**·4Cl. (B) Disordered forms of BODIPY fragments after fixing the position of the hexafluorophosphate ions. (C) Top-down and (D) side-on view of a single molecule. Illustration of the packing of **BBox**$^{4+}$ along (E) *b*-axis and (F) *c*-axis.

disproportionation reaction to generate radical intermediates for the oxidization of NADH, which promotes the intramolecular photoelectron transfer. HACD in SPR is employed as a "sponge" to enrich Dox ⊂ **BBox**·4Cl by the multivalent interaction and thus concentrates them closer together in space, which facilitates the intermolecular photoelectron transfer. Meanwhile, intracellular NADH is depleted as a sacrificial agent to replenish photoelectrons for SPR, which disturbs the intracellular redox balance and accelerates the apoptosis. As expected, Dox ⊂ **BBox**·4Cl@HACD as SPR exhibits remarkable therapeutic efficiency for tumor treatment in vitro and in vivo.

RESULTS AND DISCUSSION

Synthesis and Characterization. As shown in Figure 1A, the synthesis of **BBox**·4Cl was performed in 17% yield by a one-step S_N2 reaction of intermediate **4**·2PF_6 and 4-pyridyl substituted BODIPY (**3**) in the presence of pyrene and tetrabutylammonium iodide (TABI) as the template and catalyst, respectively. The intermediate **4**·2PF_6 and the reference compound **5**·2Cl were obtained by the S_N2 reactions of **3** with either *α*,*α*′-dibromo-para-xylene or benzyl bromide (BnBr) in 73% and 63% yield after counterion exchange, respectively (Figures S1−S6). The successful synthesis of **BBox**·4Cl was confirmed by ^{1}H NMR and ^{13}C NMR spectroscopy (Figures S7 and S8), while its high-resolution mass spectrometry (HRMS) detected the characteristic peak of $[M-3Cl]^{3+}$ at m/z = 399.8413, belonging to the typical isotopic distribution of trivalent ions (Figure S9).

By slow evaporation of diisopropyl ether into an acetonitrile solution of **BBox**·4PF_6 at room temperature for 7 days, its single crystal was obtained. The solid-state X-ray structure of **BBox**$^{4+}$ shows two kinds of disordered forms of BODIPY fragments (Figure 1B) due to the different relative positions of the hexafluorophosphate ions in the crystal. However, there is no difference in the orientation and stacking pattern in these

https://doi.org/10.1021/acs.jmedchem.5c00094
J. Med. Chem. XXXX, XXX, XXX−XXX

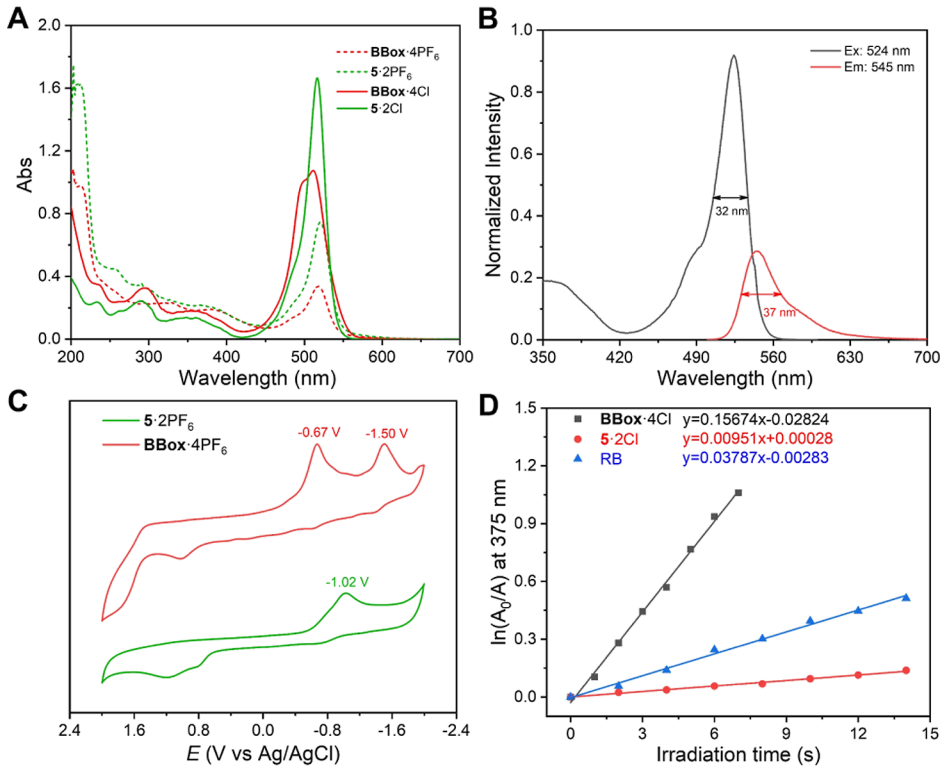

Figure 2. Optoelectronic properties of $\mathbf{BBox}^{4+}$ and reference compound $\mathbf{5}^{2+}$. (A) UV−vis spectra of **BBox**·$4PF_6$ (10 μM in CH_3CN), **5**·$2PF_6$ (20 μM in CH_3CN), **BBox**·4Cl (10 μM in H_2O), and **5**·2Cl (20 μM in H_2O). (B) Fluorescence excitation and emission spectra of **BBox**·4Cl (10 μM) in H_2O. (C) Voltammogram (scan rate: 200 mV/s) of **5**·$2PF_6$ and **BBox**·$4PF_6$ in acetonitrile solution at the concentration of 0.1 mM for BODIPY units. (D) Normalized degradation percentages of ABDA at 375 nm in the presence of **BBox**•4Cl (10 μM), **5**·2Cl (20 μM), and Rose Bengal (RB, 10 μM) after white light irradiation (220 mW/cm^2) for different time intervals using ABDA (50 μM) as the $^1O_2$ indicator.

two forms. $\mathbf{BBox}^{4+}$ has extended π-conjugated planes, where the two BODIPY units are stacked antiparallel and at a 63.4-degree angle with the plane of BODIPY. The cavity is like an opened envelope with the length and height of 18.438 and 11.908 Å, respectively, and its pyridinium units are bent inward or outward of the macrocycle, resulting in the division of the cavity into two chambers with larger and smaller widths of 8.164 and 5.793 Å (Figure 1C,D). The packing of $\mathbf{BBox}^{4+}$ displays fence-like tubular superstructures in the *b*-axis, indicating the π-stacking interactions among neighboring BODIPY planes with a distance of 4.099 Å (Figure 1E). In the *c*-axis, adjacent layers of $\mathbf{BBox}^{4+}$ are joined together via C−H···π interactions in a herringbone packing mode to form an expanded supramolecular structure (Figure 1F). Obviously, envelop-like conformation, a large π-conjugated plane, and the topological structure driven by multiple noncovalent interactions without interpenetrating behaviors favor the $\mathbf{BBox}^{4+}$ to encapsulate the size-matched guest molecules and exhibit special photophysical behaviors.

Optoelectronic Properties. The photoluminescence behaviors of BODIPY-based macrocycle $\mathbf{BBox}^{4+}$ and its reference compound **5** were investigated in water and organic solvent. As shown in Figure 2A, all compounds exhibited similar UV−vis spectra with a main absorption band ranging from 420 to 650 nm, where **5**·2Cl showed a narrower absorption peak at 517 nm while **BBox**·4Cl gave a hypsochromic shift to 511 nm, and a shoulder peak appeared at 496 nm in water. On account of the spatial proximity of the chromophores,[43] $\mathbf{BBox}^{4+}$ in forms of both chloride salt and hexafluorophosphate showed a significant decrease in absorption compared to its reference compound **5** despite controlling the consistent concentration of chromophores. The excitation and emission spectra of $\mathbf{BBox}^{4+}$ and compound **5** in the forms of chloride salt and hexafluorophosphate were then conducted in water and acetonitrile, respectively (Figures 2B, S10, and S11). All species showed narrow-band emission (full width at half maxima below 37 nm) in the wavelength range of 500−700 nm, with maximum emission peaks of 541−547 nm. In addition, the quantum yields of **5**·$2PF_6$ and **BBox**·$4PF_6$ were obtained as 82.98% and 34.15% in acetonitrile, respectively (Figure S12). However, the quantum yields of **5**·2Cl and **BBox**·4Cl were determined as 80.34% and 5.34% in water (Figure S13), respectively. This remarkable decrease in quantum yields for **BBox**·4Cl in water may be attributed to the enhanced self-assembly driven by π-stacking interactions, which was further confirmed by the ^{1}H NMR spectra of **5**·2Cl and **BBox**·4Cl at low (1 mM for BODIPY units) and high (10 mM for BODIPY units) concentrations. As shown in Figures S14 and S15, when the concentration of **BBox**·4Cl was increased from 0.5 to 5 mM, which corresponded to the concentration of 1 and 10 mM for BODIPY units, the signals of all protons (c, d, e, f, g) of BODIPY fragments and b-H on the β-position of pyridinium all went significant upshifting. In contrast, for **5**·2Cl, increasing the concentration from 1 to 10 mM failed to cause apparent shifting of the signals of protons, indicating that the BODIPY units of **BBox**·4Cl formed more stable π-stacking complexes in water than **5**·2Cl. In order to investigate the electrochemical properties of the BODIPY-based macrocycle, cyclic voltammetry was employed in acetonitrile solutions containing 0.1 M tetrabutylammonium

https://doi.org/10.1021/acs.jmedchem.5c00094
J. Med. Chem. XXXX, XXX, XXX−XXX

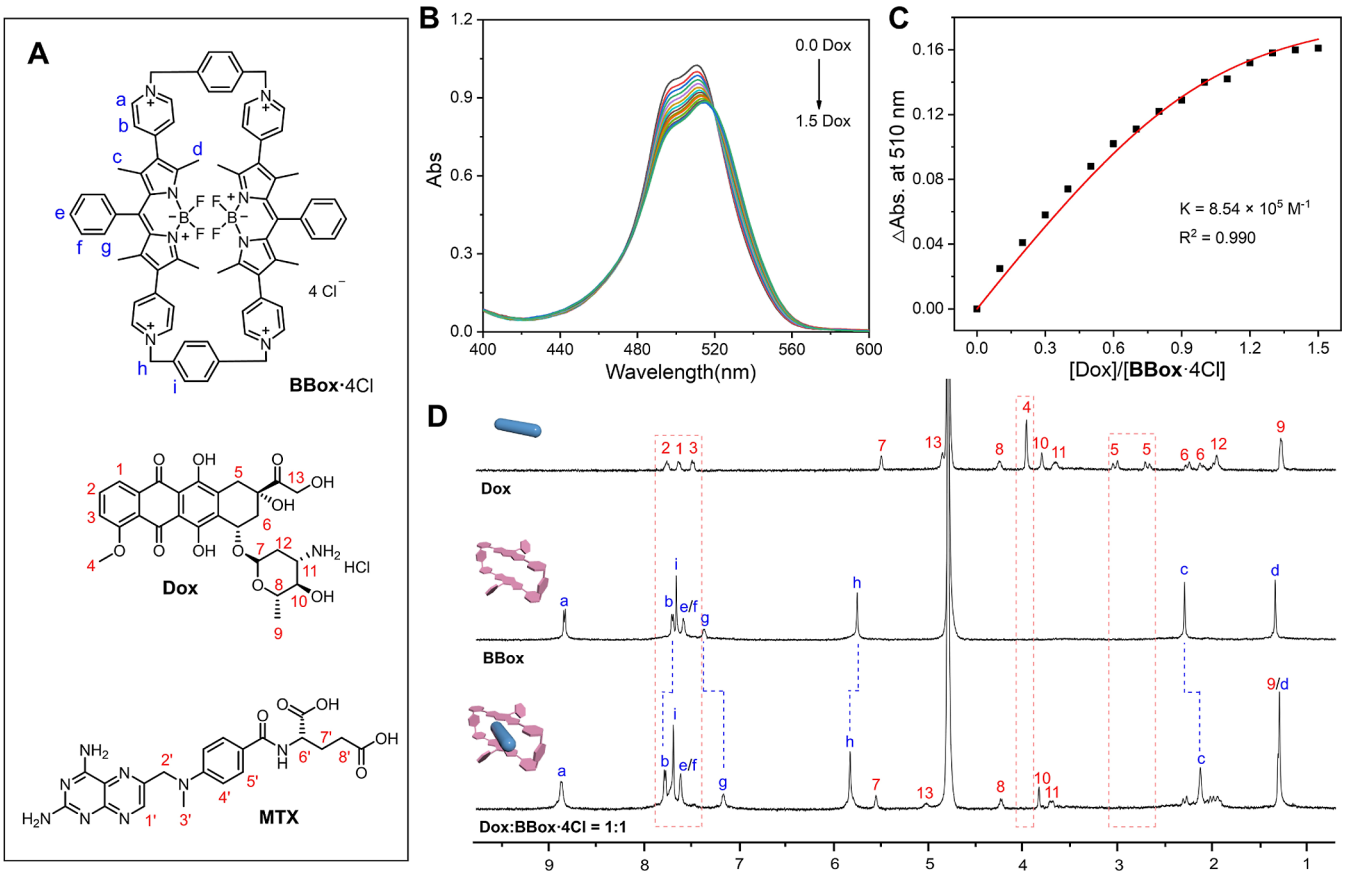

Figure 3. Host–guest behaviors between $\mathbf{BBox}^{4+}$ and Dox. (A) Chemical structures of **BBox**·4Cl, Dox, and MTX. (B) UV–vis spectra of the solution of **BBox**·4Cl (10 μM) in H_2O with the addition of Dox (0–15 μM). (C) Fitting curve for binding Dox with **BBox**·4Cl. (D) ^{1}H NMR spectra of Dox, **BBox**·4Cl, and host–guest mixture of Dox ⊂ **BBox**·4Cl at the ratio of 1:1 (400 MHz, D_2O, 298 K).

hexafluorophosphate as the supporting electrolyte (Figure 2C). The voltammogram of **BBox**·4PF_6 exhibited two reduction waves (−0.67 and −1.50 V vs Ag/AgCl), which could be assigned to the stepwise reduction of the two pyridyl BODIPY units, where the pyridinium radical species were generated from pyridinium cations by potentiostatic electrolysis. On the other hand, the voltammogram of **5**·2PF_6 showed a lower first reduction potential (−1.02 V vs Ag/AgCl), indicating that **BBox**·4PF_6 with a structure of macrocycle accepted electrons more readily than its reference compound **5**·2PF_6.

Considering that **BBox**·4Cl had a strong absorption centered at 510 nm in the visible range from 420 to 650 nm and that its radiative excursion was suppressed to quench the fluorescence, the singlet oxygen ($^1O_2$) generation efficiency was determined by 9,10-anthracenediyl-bis(methylene)-dimalonic acid (ABDA) used as an indicator for $^1O_2$ and the change of UV–vis absorbance at 375 nm plotted against time (Figure S16). ABDA was stable even when it was exposed to light irradiation for 10 min (Figure S17). As shown in Figure 2D, the photodegradation of ABDA in the presence of **BBox**·4Cl tended to be complete within 7 s, and the $^1O_2$ generation rate of **BBox**·4Cl was significantly higher than the standard RB and its reference molecule **5**·2Cl. The $^1O_2$ quantum yield of **BBox**·4Cl was determined as 160%, which was a 2.1 and 17.8-fold increase compared to that of the standard RB (75%) and **5**·2Cl (9%), respectively (Table S1). These results were consistent with the reduced fluorescence intensity of **BBox**·4Cl and further confirmed that the stacking pattern of **BBox**·4Cl in water facilitated the intersystem crossing of the photosensitizer in the excited singlet state to the triplet state and suppressed energy loss due to the radiative transition.

Supramolecular Cascade Assembly. Possessing envelope-like cavities with large π-conjugate planes, **BBox**·4Cl can effectively hinder the escape of guest molecules. Given its excellent ability to generate $^1O_2$ in the visible light region, the host–guest binding behaviors of **BBox**·4Cl with two neutral antitumor drugs, doxorubicin (Dox), and methotrexate (MTX) were explored by UV–vis and NMR spectroscopy (Figure 3A). A significant decrease in absorption centered at 510 nm was observed as the concentration of Dox or MTX in the host–guest mixture solution gradually increased. Once the concentration of Dox or MTX was equal to or exceeded that of **BBox**·4Cl, the characteristic absorption band slowly decreased and tended to be stable (Figures 3B and S18a). Remarkably, the addition of Dox induced a significant bathochromic shift (~5 nm) in the UV–vis absorption peak of **BBox**·4Cl. These observations indicated that Dox and MTX were encapsulated within the cavity of **BBox**·4Cl. The 1:1 stoichiometric binding ratio between **BBox**·4Cl and either Dox or MTX was confirmed through Job's plot experiments, based on the maximum absorbance change at a molar fraction of 0.5 (Figure S19). Furthermore, UV titration experiments were performed, yielding an association constant (K) of 8.05 × 10^5 M^{-1} and 8.54 × 10^5 M^{-1} for the host–guest complexes, Dox ⊂ **BBox**·4Cl and MTX ⊂ **BBox**·4Cl, respectively, calculated by a nonlinear least-squares formula (Figures 3C and S18b). ^{1}H NMR spectroscopy was then employed to identify the binding sites between **BBox**·4Cl and Dox or MTX. As shown in Figure

https://doi.org/10.1021/acs.jmedchem.5c00094
J. Med. Chem. XXXX, XXX, XXX–XXX

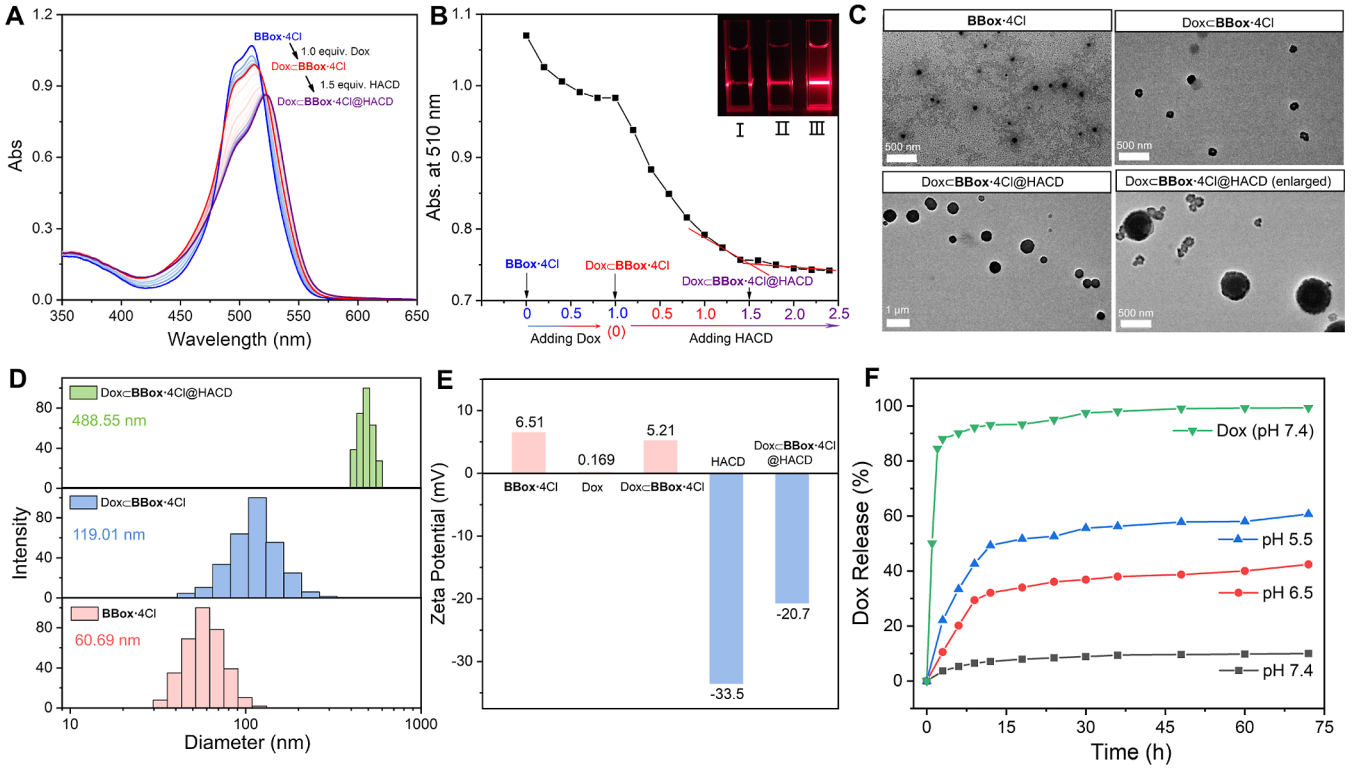

Figure 4. Characterization of the cascade assembly process. (A) UV−vis spectra and (B) changes in absorbance at 510 nm of **BBox**·4Cl (10 μM) with the sequential addition of Dox (0−10 μM) and HACD (0−24 μM). Insert: the Tyndall effects in the solution of Dox ⊂ **BBox**·4Cl (I), HACD (II), and Dox ⊂ **BBox**·4Cl@HACD (III). (C) TEM images, (D) DLS analysis, and (E) zeta potentials of **BBox**·4Cl (10 μM), Dox ⊂ **BBox**·4Cl (10 μM), and Dox ⊂ **BBox**·4Cl@HACD (10 μM). (F) Dialysis of the Dox ⊂ **BBox**·4Cl@HACD solution (1 mM, 2 mL) to buffer solution (30 mL) at 37 °C (molecular weight cutoff: 1000 Da).

3D, the signals of c- and g-H of **BBox**·4Cl underwent significant upshifting and 1−5 H of Dox broadened and then disappeared, while the signals of b and h−H of **BBox**·4Cl shifted downfield, indicating that the anthracycline units of Dox entered the cavity of **BBox**·4Cl and stacked with the inner BODIPY units. Similarly, for MTX (Figure S20), upfield shifts were observed for the 1′-H of the pterin moiety, 4′,5′-H of the benzene ring, and the 2′,3′-H of the aminomethyl linker, indicating that the pterin and benzene units were confined within the **BBox**·4Cl cavity. These findings demonstrated that the appropriate size, π-conjugated cavity, and envelope-like structure of **BBox**·4Cl make it a promising candidate for drug delivery.

Although **BBox**·4Cl had a high affinity for both Dox and MTX, Dox ⊂ **BBox**·4Cl was selected for further study of the $\mathbf{BBox}^{4+}$-mediated drug loading system and therapeutic capacity due to higher water solubility. In pursuit, β-CD-grafted hyaluronic acid (HACD) with abundant negative charge was utilized for the secondary encapsulation of Dox ⊂ **BBox**·4Cl through electrostatic interaction, forming three-component nanoparticles capable of targeting overexpressed receptors such as cluster determinant 44 (CD44) and HA-mediated motility receptor (RHAMM) on the surfaces of various tumor cells.[44−46] The substitution degree of the β-cyclodextrin (β-CD) was determined as 10% by comparing the integral area of 1 H (1.97 ppm) and 2 H (5.04 ppm), corresponding to the characteristic signals of the HA moiety and β-CD moiety, respectively (Figure S21). The secondary assembly process of Dox ⊂ **BBox**·4Cl with HACD was investigated by UV−vis (Figure 4A,B) and fluorescence spectroscopy (Figure S22). For **BBox**·4Cl, the absorbance at 510 nm and fluorescence intensity at 545 nm were decreased with the stepwise addition of Dox and reached equilibrium at a 1:1 stoichiometry. Continuing to add HACD to the 1:1 mixture of **BBox**·4Cl and Dox, further significant decreases in absorbance and fluorescence intensity were observed, and it was almost in equilibrium when increasing the amount of HACD to 1.5 equiv (calculated by β-CD units). Meanwhile, a significant Tyndall effect could also be observed in the Dox ⊂ **BBox**·4Cl@HACD solution (Figure 4B, inset), indicating the formation of supramolecular nanoassemblies. Subsequently, transmission electron microscopy (TEM), field emission scanning electron microscope (FE-SEM), dynamic light scattering (DLS), and zeta potential experiments were employed to characterize the morphology of Dox ⊂ **BBox**·4Cl@HACD. The TEM images of **BBox**·4Cl and Dox ⊂ **BBox**·4Cl showed near-spherical nanoparticles with average sizes of 58.20 and 136.26 nm, respectively, while Dox ⊂ **BBox**·4Cl@HACD presented spherical nanoparticles with varying sizes of 315−600 nm (Figure 4C). Remarkably, the enlarged TEM image of Dox ⊂ **BBox**·4Cl@HACD showed the process of self-assembly, suggesting that the reason for the different sizes of Dox ⊂ **BBox**·4Cl@HACD may be that the larger assemblies were further assembled from the smaller ones, as well as Dox ⊂ **BBox**·4Cl@HACD was assembled from HA with different lengths or molecular weights. Similarly, the FE-SEM image further revealed that Dox ⊂ **BBox**·4Cl@HACD was a spherical nanoparticle (Figure S23). DLS measurements also demonstrated that the effective hydrodynamic diameters of **BBox**·4Cl, Dox ⊂ **BBox**·4Cl, and Dox ⊂ **BBox**·4Cl@HACD were 60.69,

https://doi.org/10.1021/acs.jmedchem.5c00094
J. Med. Chem. XXXX, XXX, XXX−XXX

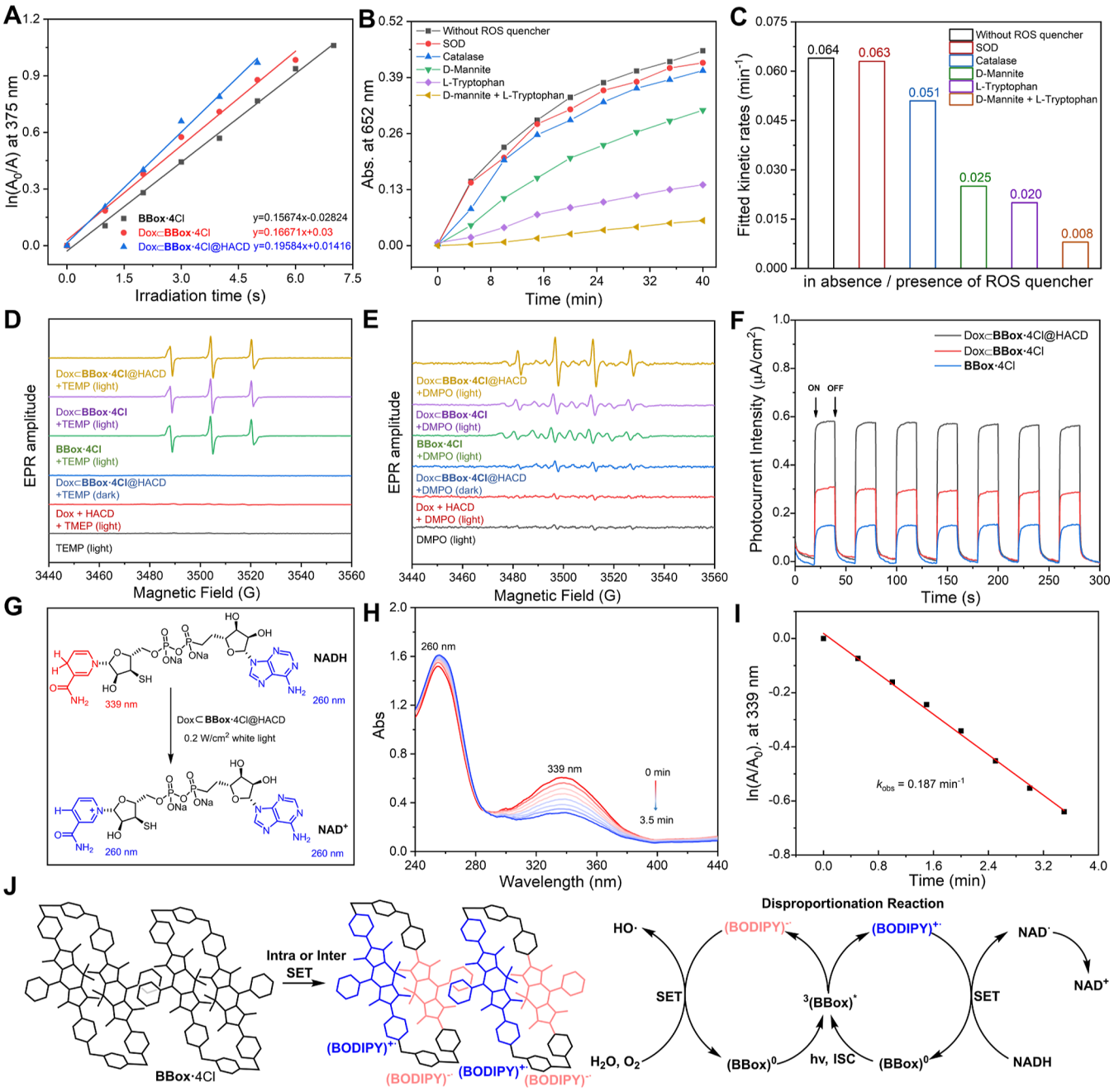

Figure 5. Evaluation of the supramolecular assembly photodynamic effect. (A) Normalized degradation percentages of ABDA at 375 nm in the presence of **BBox**·4Cl (10 μM), Dox ⊂ **BBox**·4Cl (10 μM), and Dox ⊂ **BBox**·4Cl@HACD (10 μM) after white light irradiation (220 mW/cm^2) for different time intervals using ABDA (50 μM) as the $^1O_2$ indicator. (B) Absorbance of oxidized TMB at 652 nm in the mixture of Dox ⊂ **BBox**·4Cl@HACD (10 μM) and different ROS quenchers after white light irradiation (220 mW/cm^2) for different time intervals using TMB (100 μM) as the ROS indicator. (C) Fitted apparent first-order kinetic constants for the oxidation of TMB in the presence of different ROS quenchers. EPR spectra to detect $^1O_2$ (D) and $^{\bullet}$OH (E) generated by **BBox**$^{4+}$ species (0.1 mM) under white light irradiation (220 mW/cm^2, 30 s), using TMEP (0.3 M) and DMPO (45 mM) as a spin-trap agent. (F) Representative photocurrent responses of **BBox**·4Cl and Dox ⊂ **BBox**·4Cl@HACD on the ITO plate electrode with the interval of 30 s. (G) Schematic illustration of photocatalytic oxidation of NADH by Dox ⊂ **BBox**·4Cl@HACD. (H) UV−vis spectra of NADH (100 μM) in the presence of Dox ⊂ **BBox**·4Cl@HACD (10 μM) and (I) plots of ln(A/A$_0$) of NADH at 339 nm after white light irradiation (220 mW/cm^2) for different time intervals. (J) Mechanism of the photoinduced $^{\bullet}$OH generation in type-I PDT.

119.01, and 488.55 nm, respectively, which matched well with the TEM results (Figure 4D). In addition, as depicted in Figures 4E and S24, the tetracationic **BBox**·4Cl exhibited a zeta potential of 6.51 mV, which decreased slightly to 5.21 mV after assembly with Dox (0.169 mV). The zeta potential of Dox ⊂ **BBox**·4Cl@HACD was converted to −20.7 mV upon further assembly with HACD (−33.5 mV). All of the experimental results indicated that the binary complex Dox ⊂ **BBox**·4Cl could undergo secondary assembly with HACD by the electrostatic interaction to form negatively charged spherical nanoparticles.

Subsequently, dialysis experiments were conducted at different pH values to explore the deconstruction of nanoparticles and the release of Dox under various complex

https://doi.org/10.1021/acs.jmedchem.5c00094
J. Med. Chem. XXXX, XXX, XXX−XXX

physiological conditions. As shown in Figure 4F, Dox ⊂ **BBox**·4Cl@HACD allowed for less than 10% of Dox released into the external solution after 72 h at the normal physiological pH of 7.4, suggesting that the nanoparticles could undergo circulation in normal blood plasma. However, when nanoparticles were exposed to weakly acidic tumor tissue (pH = 6.5) as well as more acidic endosomal or lysosomal compartments (pH = 5.5), the release rate of Dox reached 42% and 60% after 72 h, respectively. All the results showed that Dox ⊂ **BBox**·4Cl@HACD allowed for the release of Dox at the specific tumor sites with an acidic environment, which might be attributed to the loss of negative charge density in HACD, accompanied by the partial disassembly of the nanoparticles.

Supramolecular Assembly Photodynamic Effect. After examination of the binary complex Dox ⊂ **BBox**·4Cl and the three-component assembly Dox ⊂ **BBox**·4Cl@HACD, their $^1O_2$ quantum yields were determined through the photodegradation of ABDA (Figures 5A, S25 and Table S2). The results suggested that both assemblies retained their robust $^1O_2$ generation capability. Excitingly, Dox ⊂ **BBox**·4Cl@HACD was also found to produce $^{\bullet}$OH through a hypoxia-tolerant electron transfer mechanism, enabling PDT to function effectively in oxygen-deficient tumor tissue. The generation of $^{\bullet}$OH was monitored by the control experiments in the presence of 3,3,5′,5′-tetramethylbenzidine (TMB), which could be oxidized by ROS[47] generated from Dox ⊂ **BBox**·4Cl@HACD under irradiation with the enhanced absorption at 652 nm (Figure S26). A series of ROS quenchers, including L-tryptophan (for $^1O_2$), D-mannitol (for $^{\bullet}$OH), catalase (for H_2O_2), and superoxide dismutase (SOD, for superoxide), were then added to the mixture of Dox ⊂ **BBox**·4Cl@HACD and TMB to inhibit the oxidation of TMB. As depicted in Figures S27−S31, both L-tryptophan and D-mannitol were able to partially quench the absorption of oxidized TMB, leading to the decrease of fitted apparent first-order kinetic constants (K_{obs}) from 0.064 min^{-1} to 0.025 and 0.02 min^{-1}, respectively. When both quenchers were added together, TMB oxidation was nearly completely inhibited with K_{obs} as low as 0.008 min^{-1} (Figure 5B,C). These results confirmed that both $^1O_2$ and $^{\bullet}$OH were generated in the Dox ⊂ **BBox**·4Cl@HACD solution upon irradiation. The electron paramagnetic resonance (EPR) further validated the generation of both $^1O_2$ and $^{\bullet}$OH in the photodynamic system. Using 2,2,6,6-tetramethyl-4-piperidinone (TEMP) as the spin-trap agent, characteristic signals of the TEMP-$^1O_2$ adduct were observed in irradiated solutions of **BBox**·4Cl, Dox ⊂ **BBox**·4Cl, and Dox ⊂ **BBox**·4Cl@HACD, with comparable amplitudes (Figure 5D), which matched well with the results of the photodegradation experiments. Likewise, 5,5-dimethyl-1-pyrroline *N*-oxide (DMPO) was selected as the spin-trap agent for $^{\bullet}$OH and the characteristic signals of the DMPO-$^{\bullet}$OH adduct were observed after irradiation, in which the amplitudes increased gradually with the addition of Dox and HACD (Figure 5E), indicating the cascaded assembly effectively enhanced the $^{\bullet}$OH generating capacity of **BBox**·4Cl and promoted the type-I photodynamic process. In addition, as expected, Dox ⊂ **BBox**·4Cl@HACD also exhibited a significantly enhanced photocurrent intensity as compared to **BBox**·4Cl and Dox ⊂ **BBox**·4Cl (Figure 5F), which further illustrated that Dox and HACD, participating in nanosupramolecular assembly as antitumor drug and targeting agent, respectively, showed additional contributions to the electron transfer and the generation of $^{\bullet}$OH for **BBox**·4Cl.

NADH, as a coenzyme playing a vital role in maintaining the intracellular redox balance[48] by the interconversion with NAD^+, was considered as a sacrificial agent in the process of electron transfer and facilitated the electron recycling in type-I PDT. In order to confirm this mechanism, the consumption of NADH was monitored by UV−vis spectroscopy (Figures 5G,H). Upon irradiating the solution of NADH containing Dox ⊂ **BBox**·4Cl@HACD, the characteristic absorption of NADH at 339 nm decreased significantly, and the rate constant (k_{obs}) of NADH oxidation was calculated to be 0.187 min^{-1} (Figure 5I). Further verification of NADH oxidation was performed using ^{1}H NMR spectroscopy, where the characteristic signals of NAD^+ intensified, and those of NADH diminished within 20 min in the presence of Dox ⊂ **BBox**·4Cl@HACD as the catalyst (Figure S32). In the absence of Dox ⊂ **BBox**·4Cl@HACD, no significant changes were observed (Figure S33). These findings indicated that Dox ⊂ **BBox**·4Cl@HACD could effectively catalyze NADH oxidation and facilitate the continuous electron flow from NADH during irradiation.

As shown in Figure 5J and Figure S34, the photoinduced generation of $^1O_2$ and $^{\bullet}$OH involved an energy transfer and electron transfer process, respectively. The triplet excited photosensitizer ^{3}(**BBox**)* formed by the intersystem crossing from the excited singlet state has a longer lifetime and facilitates the occurrence of energy transfer and electron transfer with oxygen. On the one hand, ^{3}(**BBox**)* directly undergoes energy transfer with oxygen to generate $^1O_2$, which remains unaffected by host−guest interaction or secondary assembly, ensuring a stable type-II photodynamic effect. On the other hand, rapid electron transfer occurs in two opposing BODIPY units of ^{3}(**BBox**)*, and a pair of free radical ions, $(BODIPY)^{\bullet+}$ and $(BODIPY)^{\bullet-}$, are generated through a photoinduced intramolecular or intermolecular disproportionation reaction.[49] The radical anion $(BODIPY)^{\bullet-}$ transfers an electron to dissolved oxygen, producing $^{\bullet}$OH, while the radical cation $(BODIPY)^{\bullet+}$ accepts electrons from NADH. More importantly, as demonstrated above, NADH was successfully converted to NAD^+ by catalytic oxidation, and Dox ⊂ **BBox**·4Cl@HACD can be considered a photoelectron "reservoir" in this photoredox system. In detail, this photoelectron "reservoir" constructed by the supramolecular cascade assembly can continuously grasp electrons from NADH as the sacrificial agent by catalytic oxidation, store electrons as radical forms, and further pump them to oxygen, thereby realizing the harvest of $^{\bullet}$OH and the conversion of the type-II PDT into type-I PDT. In addition, the contribution of the two components of photocatalyst, Dox and HACD, to photoelectron transfer and $^{\bullet}$OH generation discussed above can be visualized by the concepts of "pump" and "sponge" to reflect their roles played in "reservoir". On the one hand, Dox is encapsulated by **BBox**·4Cl and is exactly located in the cavity formed by the opposing BODIPY units, which can help to pump electrons between two sides of BODIPY units to mediate intramolecular electron transfer in **BBox**·4Cl. On the other hand, HACD can enrich and spatially align Dox ⊂ **BBox**·4Cl to facilitate the intermolecular electron transfer in **BBox**·4Cl. This synergistic interaction significantly enhances the electron recycling efficiency, boosting the $^{\bullet}$OH generation capacity of Dox ⊂ **BBox**·4Cl@HACD.

https://doi.org/10.1021/acs.jmedchem.5c00094
J. Med. Chem. XXXX, XXX, XXX−XXX

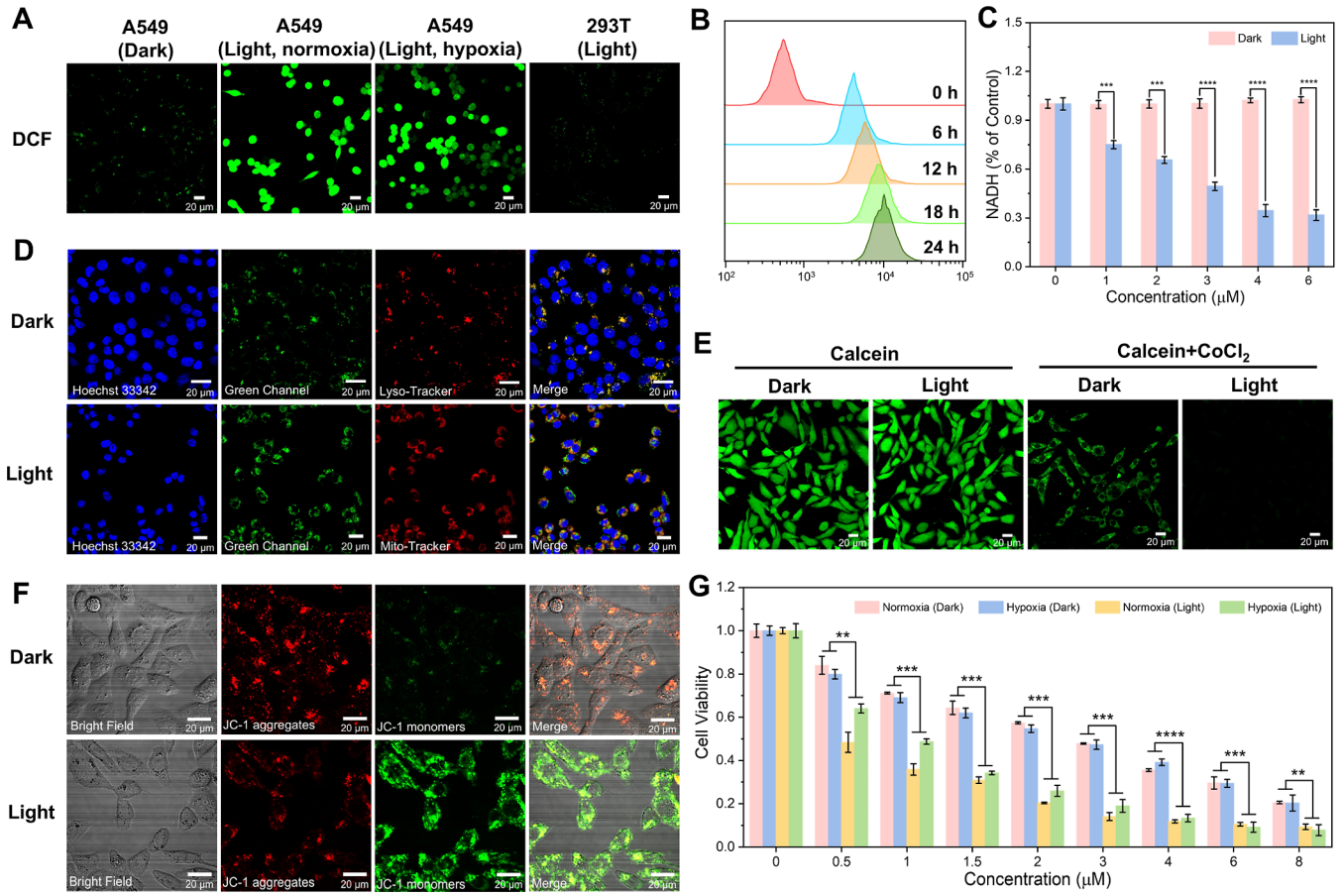

Figure 6. PDT in vitro after treatment with Dox ⊂ **BBox**·4Cl@HACD. (A) Detection of intracellular total levels of $^1O_2$ and $^\bullet$OH in A549 cells and 293T cells with Dox ⊂ **BBox**·4Cl@HACD (0.5 μM) and DCFH-DA (10 μM) after different treatment. (B) Flow cytometry profile for A549 cells treated with Dox ⊂ **BBox**·4Cl@HACD (2 μM) for different time intervals. (C) Detection of intracellular NADH level with the addition of Dox ⊂ **BBox**·4Cl@HACD (0−6 μM) under dark and white light irradiation (220 mW/cm^2, 10 min) by NAD$^+$/NADH assay kit. (D) Confocal microscopy images of LysoTracker Red or MitoTracker Red stained A549 cells in the presence of Dox ⊂ **BBox**·4Cl@HACD (2 μM) under dark and white light irradiation (220 mW/cm^2, 10 min). (E) Confocal microscopy images of calcein/$CoCl_2$-stained A549 cells in the presence of Dox ⊂ **BBox**·4Cl@HACD (0.5 μM) under dark and white light irradiation (220 mW/cm^2, 10 min). (F) Confocal microscopy images of JC-1-stained A549 cells in the presence of Dox ⊂ **BBox**·4Cl@HACD (0.5 μM) under dark and white light irradiation (220 mW/cm^2, 10 min). (G) Cell viability of A549 cells treated with Dox ⊂ **BBox**·4Cl@HACD (0−8 μM) under normoxia and hypoxia in the absence/presence of white light irradiation (220 mW/cm^2, 10 min). Data presented were the means ± standard error of the mean. $^{**}p < 0.01$, $^{***}p < 0.001$, and $^{****}p < 0.0001$.

PDT In Vitro. Given that the **BBox**$^{4+}$ species were capable of simultaneous photoinduced energy transfer and electron transfer, we focused on the PDT process of the preferred photosensitizer Dox ⊂ **BBox**·4Cl@HACD in vitro. First, flow cytometry was employed to evaluate the cell uptake of Dox ⊂ **BBox**·4Cl@HACD, and the results showed that it was effectively internalized by A549 human lung adenocarcinoma cells, approached the peak at around 12 h, and was retained in cells for at least another 12 h (Figures 6B and S35). After confirmation that Dox ⊂ **BBox**·4Cl@HACD could effectively be taken up by cells, the generation of $^1O_2$ and $^\bullet$OH and the involvement of NADH in the photodynamic system were further validated at the cellular level. The commercially available probe 6-carboxyl-2′,7′-dichlorodihydrofluorescein diacetate (DCFH-DA) was internalized into A549 cells and 293T human embryonic kidney cells to investigate the intracellular total levels of $^1O_2$ and $^\bullet$OH under light irradiation. As discerned from Figure 6A, the A549 cells manifested bright green fluorescence in both normoxia and hypoxia after irradiation, whereas the control group without irradiation showed only weak green fluorescence, indicating the intracellular $^1O_2$ and $^\bullet$OH generation upon irradiation. Meanwhile, due to the lack of HA-mediated endocytosis, the 293T cells failed to display obvious fluorescence signals. The NADH depletion in A549 cells was assessed by the NAD$^+$/NADH assay kit with WST-8. As shown in Figure 6C, the effect of light irradiation on the levels of NADH was negligible in the absence of Dox ⊂ **BBox**·4Cl@HACD. Intracellular levels of NADH decreased with the increasing concentrations of Dox ⊂ **BBox**·4Cl@HACD under light irradiation, whereas NADH was virtually unaffected in the absence of light irradiation, suggesting that NADH as the sacrificial agent was consumed for the replenishment of photoelectron in SPR.

Subsequently, the distribution of Dox ⊂ **BBox**·4Cl@HACD in the organelles of A549 cells was observed by laser scanning confocal microscopy (LSCM) (Figure 6D). The green fluorescence of Dox ⊂ **BBox**·4Cl@HACD overlapped well with the red signal of LysoTracker Red after 12 h incubation, and the Pearson correlation coefficient was accordingly calculated as 0.91 (Figure S36). However, Dox ⊂ **BBox**·4Cl@HACD underwent migration from lysosomes to mitochondria, and the Pearson correlation coefficient for

https://doi.org/10.1021/acs.jmedchem.5c00094
J. Med. Chem. XXXX, XXX, XXX−XXX

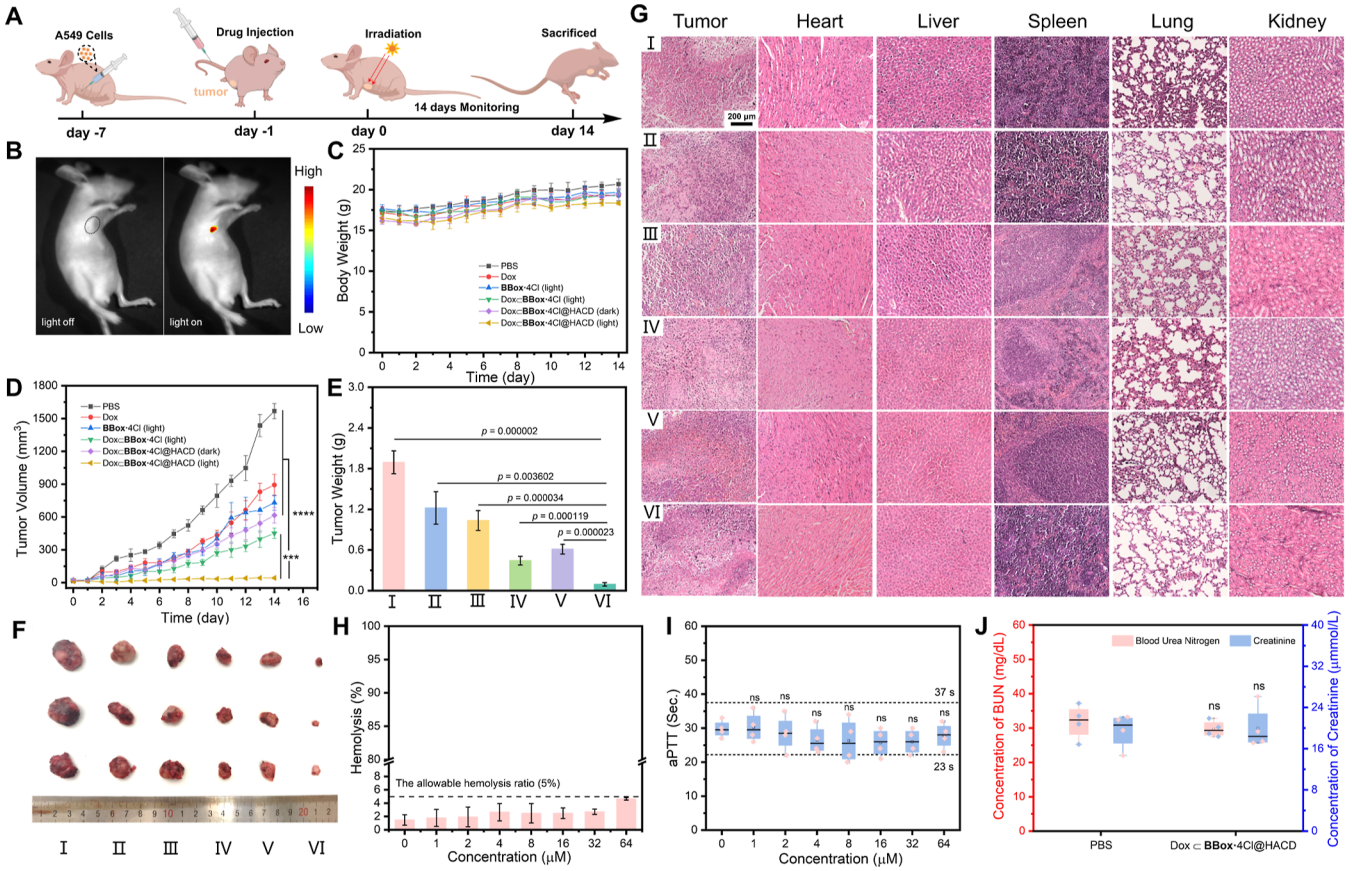

Figure 7. PDT in vivo and biosafety evaluation after treatment with Dox ⊂ **BBox**·4Cl@HACD. (A) Schematic illustration of the in vivo PDT process with the tumor-bearing mice model. (B) In vivo fluorescence images of mice treated with Dox ⊂ **BBox**·4Cl@HACD. (C) Body weights, (D) tumor volumes, (E) average tumor weights, and (F) representative photographs of tumors of the mice in different groups in 14 days after treatment. (G) H&E staining images of tumor tissues from different samples of tumor-bearing mice. (H) Hemolytic activity of rabbit erythrocyte and (I) activated partial thromboplastin time (aPTT) assays in rabbit plasma for the clotting time vary with the amount of Dox ⊂ **BBox**·4Cl@HACD. (J) Concentration of blood urea nitrogen (BUN) and creatinine (Cr) of fresh extracted plasma after mice treated with PBS and Dox ⊂ **BBox**·4Cl@HACD. (I) PBS, (II) Dox, (III) **BBox**·4Cl + light, (IV) Dox ⊂ **BBox**·4Cl + light, (V) Dox ⊂ **BBox**·4Cl@HACD, and (VI) Dox ⊂ **BBox**·4Cl@HACD + light. Data presented were the means ± SEM ***p < 0.001, ****p < 0.0001, n.s. was represented for nonsignificant.

mitochondria was determined as 0.73 after white light irradiation (Figure S37). In order to investigate the mechanism of migration, the mitochondrial membrane potential assay kit with JC-1 and the mitochondrial permeability transition pore (MPTP) assay kit with calcein/$CoCl_2$ were both employed to assess the effect of Dox ⊂ **BBox**·4Cl@HACD on mitochondrial morphology. Taking advantage of the properties of JC-1 in the forms of aggregates with red fluorescence and monomers with green fluorescence at high and low mitochondrial potentials, respectively, the changes of mitochondrial potentials can be detected to reflect the degree of mitochondrial depolarization. As shown in Figure 6F, the green fluorescence representing JC-1 monomers was significantly enhanced in A549 cells ingesting Dox ⊂ **BBox**·4Cl@HACD after light irradiation, illustrating the decrease of the degree of mitochondrial depolarization. Furthermore, calcein with green fluorescence can accumulate in cytosolic compartments, including mitochondria, while $CoCl_2$ can selectively quench the cytosolic fluorescence except in the mitochondria due to the close of MPTP in normal. As depicted in Figure 6E, after A549 cells administrated Dox ⊂ **BBox**·4Cl@HACD were treated with calcian and $CoCl_2$ sequentially, the green fluorescence of calcein in mitochondria was maintained but completely disappeared upon irradiation, demonstrating that the generation of ROS stimulated the opening of MPTP, thereby permitting $CoCl_2$ to cross the mitochondrial membrane to quench its internal fluorescence. These results suggested that Dox ⊂ **BBox**·4Cl@HACD entered the lysosomes first, and subsequent migration was attributed to the positive regulatory effect of mitochondrial permeability transition in the initial stages of treatment, and then Dox ⊂ **BBox**·4Cl@HACD consumed NADH in mitochondria, which disturbed the redox balance and triggered the further apoptosis.

Encouraged by the result that Dox ⊂ **BBox**·4Cl@HACD could generate oxygen-independent $^{\bullet}OH$ through cascade-activated electron transfer, the antitumor activity of Dox ⊂ **BBox**·4Cl@HACD was investigated under normoxia and hypoxia in A549 cells, and the cell viability was evaluated by the CCK-8 assay kit (Figure 6G). Dox ⊂ **BBox**·4Cl@HACD without light irradiation showed only the toxicity of Dox itself with a half-maximal inhibitory concentration (IC_{50}) of 2.49 μM under normoxia and 2.37 μM under hypoxia, which was close to the IC_{50} of Dox alone (Figure S38, 2.01 μM). However, the cytotoxicity of Dox ⊂ **BBox**·4Cl@HACD was significantly increased after light irradiation with IC_{50} as low as 0.46 μM under normoxia and 0.85 μM under hypoxia, which were 5.41-fold and 2.79-fold decreases, respectively, compared

https://doi.org/10.1021/acs.jmedchem.5c00094
J. Med. Chem. XXXX, XXX, XXX−XXX

to those without light treatment. These results reflected that Dox ⊂ **BBox**·4Cl@HACD achieved hypoxia-tolerant type-I/II combined PDT in vitro. The cytotoxicity of **BBox**·4Cl alone was also investigated to explore the synergistic antitumor effect between PDT and chemotherapy with Dox. As shown in Figure S39, in the absence of light irradiation, **BBox**·4Cl had no cytotoxicity to A549 cells in all of the above therapeutic concentrations, while the toxicity of **BBox**·4Cl increased dramatically after light treatment, with the values of IC_{50} reaching 2.26 and 5.31 μM under normoxic and hypoxic conditions, respectively. Accordingly, the combination indexes (CI) between Dox and photosensitizer **BBox**·4Cl under normoxia and hypoxia were calculated to be 0.43 and 0.58, respectively, indicating the high synergistic effect ($0.4 \leq CI < 0.6$) between chemotherapy and PDT in this system. Compared with other BODIPY-based photosensitizers (Table S3), this highly synergistic tumor treatment system was not only distinctively designed as a macrocyclic BODIPY-based container for targeted drug delivery but also enabled special supramolecular cascade assembly-activated $^{\bullet}OH$ generation with considerable therapeutic efficiency.

PDT In Vivo. Considering that Dox ⊂ **BBox**·4Cl@HACD exhibited excellent antitumor activity driven by multiple apoptotic mechanisms at the cellular level, the PDT efficiency was investigated with a subcutaneous tumor model of A549 cells in BALB/c nude mice (Figure 7A). Dox ⊂ **BBox**·4Cl@HACD (1.7 mM, 100 μL) or its reference drugs, including Dox, **BBox**·4Cl, and binary complex Dox ⊂ **BBox**·4Cl were administered to the mice by tail vein injection, and the tumor sites were irradiated by white light (220 mW/cm^2) after 24 h of incubation in the dark. As expected, the enrichment of Dox ⊂ **BBox**·4Cl@HACD in tumor tissue could be observed in an in vivo image due to the tumor-targeted capacity of HACD (Figure 7B). The body weights and tumor volumes of the mice were monitored for 14 days (Figure 7C,D). All experimental groups had a slight decline in body weights within 1−2 days after administration, followed by a steady weight increase during the subsequent 12 days, indicating the negligible systemic cytotoxicity of Dox ⊂ **BBox**·4Cl@HACD and its reference drugs at the therapeutic concentrations. Compared with the phosphate buffered saline (PBS) group, all treated groups showed significant tumor suppression (Figure 7D−F). Among them, the tumor growth inhibition (TGI) value of the group treated with Dox ⊂ **BBox**·4Cl@HACD and light reached 95%, which was much higher than the control groups, including Dox (36%) or **BBox**·4Cl (45%) alone, dark (68%), and nontargeted (77%). All the above results suggested that Dox ⊂ **BBox**·4Cl@HACD has potent antitumor activity with negligible systemic cytotoxicity, which benefits from the highly efficient generation of $^1O_2$ and $^{\bullet}OH$, synergistic therapy, and tumor targeting.

Biocompatibility and Safety Evaluation. When the in vivo experiment was terminated, the tumor-bearing mice were sacrificed, and the hematoxylin and eosin (H&E) staining of major organs and tumor tissues was performed. As depicted in Figure 7G, there was no obvious tissue damage or pathological variation in all treatment groups, demonstrating the high biocompatibility and safety of drugs, including Dox ⊂ **BBox**·4Cl@HACD. Meanwhile, hemolysis and aPTT assays (Figure 7H,I) in vitro showed no significant risk of hemolysis or interference with coagulation mechanisms even at 8 times the maximum administrated dose of Dox ⊂ **BBox**·4Cl@HACD. In addition, both blood urea nitrogen and creatinine assays revealed that the renal function was normal in the treatment group (Figure 7J). All of the results above further confirmed that Dox ⊂ **BBox**·4Cl@HACD has superior biocompatibility and safety for practical tumor treatment.

CONCLUSIONS

In summary, a supramolecular photoelectron "reservoir" (SPR) was designed, utilizing a BODIPY-based tetracationic macrocycle (**BBox**·4Cl) as the photosensitizer, doxorubicin (Dox) as a guest drug molecule, and tumor-targeted HACD for efficient and hypoxia-tolerant type-I/II combined PDT with cascade-activated $^{\bullet}OH$ generation capacity. **BBox**·4Cl in SPR, not only captured electrons from NADH through catalytic oxidation and transferred these electrons to oxygen for $^{\bullet}OH$ generation, but also utilized Dox and HACD as a "pump" and "sponge", respectively, to enhance both intramolecular and intermolecular photoelectron transfer, thereby facilitating the photoelectron recycling in SPR to boost the generation of $^{\bullet}OH$. Meanwhile, NADH in situ within the tumor acted as a sacrificial agent to replenish photoelectrons in SPR, thereby disrupting the normal redox balance and inducing apoptosis. Driven by various apoptotic mechanisms, Dox ⊂ **BBox**·4Cl@HACD as SPR demonstrated excellent antitumor activity, with an IC_{50} as low as 0.46 μM under normoxia and 0.85 μM under hypoxia in vitro, along with tumor growth inhibition up to 95% in vivo. This work shows a facile strategy for supramolecular cascade-activated photoelectron transfer to boost the type-I PDT process and paves the way for the exploration of in situ biological substrate-driven photoelectron recycling to achieve multiple apoptotic mechanism-triggered synergistic tumor therapy.

EXPERIMENTAL SECTION

General Procedures. ^1H and ^{13}C NMR spectra were recorded through a Bruker AV400 instrument in the indicated solvents at 25 °C. Chemical shifts were referenced to the residual solvent peaks. HRMS (HR-MS) was recorded on a Q-TOF LC−MS in an electrospray ionization source. The high-performance liquid chromatography (HPLC) trace of **BBox**·4Cl was recorded by an Agilent 1260 Infinity II using an InfinityLab Poroshell 120 SB-C18 column (4.6 × 150 mm, 2.7 μm). HPLC chromatography was performed at 40 °C with a flow rate of 0.1 mL·min^{-1}. The solvent system used was distilled water containing formic acid (0.1%) and HPLC-grade acetonitrile with a gradient of 65%. UV−vis data were collected on a Shimadzu UV-3600 spectrophotometer. The fluorescence spectra were collected on a JASCO FP-750 spectrometer. The excitation and emission spectra were recorded by Edinburgh Instrument FS5, and the quantum yields were measured with a 150 mm integrating ball. The TEM experiments were carried out on FEI Tecnai G2 F20 under 200 kV. Field emission scanning electron microscopy (FE-SEM) was recorded on FEI Apreo S LoVac working at an accelerating voltage of 200 eV ∼ 30 keV. The cyclic voltammetry was carried out with the BASi Epsilon electrochemical workstation. DLS investigations were recorded with a DynaPro NanoStar DLS detector. The Zeta potentials were examined on a Brookhaven ZETAPALS/BI-200SM at 298 K. The EPR experiments were employed with Bruker E580-10/12. Flow cytometry was employed with a Mindray BriCyte E6. LSCM and in vivo imaging were carried on Olympus FV1000 and CRi Maestro, respectively.

Materials. All solvents and chemicals were used as purchased without further purification. Doxorubicin (Dox) in the form of hydrochloride salt was purchased from Bidepharm Co., Ltd. (Shanghai, China). The purity of the final compound, **BBox**·4Cl, which was used for in vitro and in vivo assays, was determined to be >95% by an HPLC analysis (Figure S40). Compounds **1**,[50] **2**,[51] and **3**[52,53] were prepared according to reported methods with 2,4-

https://doi.org/10.1021/acs.jmedchem.5c00094
J. Med. Chem. XXXX, XXX, XXX−XXX

dimethylpyrrole and benzoyl chloride as the starting material. HACD was synthesized by the amide condensation reaction between sodium hyaluronate (M_w = 5000) and mono-6-deoxy-6 ethylenediamino-β-CD based on our previous work.[54] Catalase, superoxide dismutase, and aPTT assay kit were obtained from yuanye Bio-Technology Co., Ltd. (Shanghai, China). The NAD^+/NADH assay kit with the WST-8, ROS assay kit, Mito-Tracker Red CMXRos, Lyso-Tracker Red, mitochondrial membrane potential assay kit with JC-1, and MPTP assay kit with calcein/$CoCl_2$ were purchased from Beyotime Biotechnology Co., Ltd. (Shanghai, China). 2% rabbit red blood cells (RBC) in Alserver's solution were provided by SenBeiJia Biological Technology Co., Ltd. (Nanjing, China). Rabbit plasma was purchased from Hongquan Biological Science and Technology Co., Ltd. (Guangzhou, China). The blood urea nitrogen assay kit was purchased from Sangon Biotech Co., Ltd. (Shanghai, China). Creatinine assay kits were obtained from Nanjing Jiancheng Bioengineering Institute (Nanjing, China). The A549 and 293T cells were purchased from the Cell Resource Center, China Academy of Medical Science (Beijing, China).

Animals and Ethical Statement. BALB/c nude mice for tumor suppression assessment in vivo were purchased from Beijing FHK Bioscience Co. Ltd. All the animals were acclimated under standard laboratory conditions, including a ventilated room, a suitable temperature (25 ± 1 °C), controlled humidity (60 ± 5%), and a 12 h light/dark cycle. All procedures were conducted in accordance with the "Guiding Principles in the Care and Use of Animals" (China) and also assessed by the Animal Experimentation Ethics Committee of Nankai University, and the assigned approval number is 2021-SYDELL-000448.

Compound 4. α,α'-Dibromo-*p*-xylene (0.44 g, 1.7 mmol) was added to dry acetonitrile (25 mL) in a 100 mL round-bottomed three-neck flask, and the oil bath was raised to 90 °C until all of the solid was dissolved. Compound **3** dissolved in dry CH_2Cl_2 (15 mL) was added dropwise into the system in 1 h. After refluxing for 48 h, the reaction mixture was cooled to room temperature, and the solvent was removed by evaporation. The orange residues were washed with ethyl acetate (50 mL) and were dissolved in methanol (10 mL), A saturated solution of ammonium hexafluorophosphate in water was added dropwise and the precipitate formed was filtered, washed with water (20 mL × 3), and dried to afford compound **4** (0.14 g, 73%) as an orange solid. ^{1}H NMR (400 MHz, DMSO-d_6): δ 9.17 (d, J = 7.1 Hz, 4H), 8.13 (d, J = 7.0 Hz, 4H), 7.66 (d, J = 7.0 Hz, 2H), 7.62–7.51 (m, 8H), 7.50–7.46 (m, 2H), 7.43 (s, 1H), 5.81 (s, 4H), 4.71 (s, 4H), 2.62 (s, 6H), 1.42 (s, 6H). ^{13}C NMR (101 MHz, DMSO-d_6): δ ^{13}C NMR (101 MHz, DMSO-d_6): δ 155.25, 149.74, 145.06, 144.32, 141.97, 139.31, 138.90, 134.18, 133.29, 131.34, 130.08, 129.79, 129.66, 129.28, 128.60, 128.41, 127.60, 62.28, 45.45, 33.58, 13.50, 12.78. HRMS (ESI): calcd for $C_{45}H_{41}N_4BBr_2F_2$ $[M-2PF_6]^{2+}$: 399.8402; found, 399.8413.

BBox·4Cl. Compound **3** (84 mg,0.18 mmol) was dissolved in dry acetonitrile (200 mL) by sonication. Subsequently, compound **4** (200 mg, 0.18 mmol), TBAI (20 mg, 0.05 mmol), and pyrene (178 mg, 0.90 mmol) were added into the system, and the mixture was stirred at 50 °C for 7 days under a nitrogen atmosphere. Saturated $(t\text{-Bu})_4$NCl (5 mL) was added, and the dark orange precipitate was filtered, washed with acetonitrile (50 mL), and then subjected to column chromatography on silica gel (CH_3OH/H_2O/saturated NH_4Cl = 6:3:1, R_f = 0.4). The crude product was then dissolved in water (20 mL), and NH_4PF_6 was added until no new precipitate was produced. The precipitate formed was washed with H_2O (50 mL), dried, and redissolved in acetonitrile (20 mL). Saturated $(t\text{-Bu})_4$NCl was added dropwise until no new precipitate was produced. The precipitate that formed was washed with acetonitrile (50 mL) and dried to afford **BBox**·4Cl (39 mg, 17%) as a red powder. ^{1}H NMR (400 MHz, D_2O): δ 8.83 (d, J = 6.4 Hz, 8H), 7.69 (d, J = 6.5 Hz, 8H), 7.66 (s, 8H), 7.58 (s, 6H), 7.36 (s, 4H), 5.75 (s, 8H), 2.29 (s, 12H), 1.34 (s, 12H). ^{13}C NMR (101 MHz, D_2O): δ 155.25, 150.98, 146.11, 143.30, 143.09, 136.39, 133.24, 132.09, 130.30, 130.03, 129.82, 128.76, 128.09, 127.48, 64.16, 12.70, 12.42. HRMS (ESI): calcd for $C_{74}H_{66}N_8B_2F_4Cl$ $[M-3Cl]^{3+}$: 399.8402; found, 399.8413.

5·2Cl. Compound **3** (0.1 g, 0.21 mmol) and benzyl bromide (248 μL, 2.1 mmol) were dissolved in dry acetonitrile (40 mL) and refluxed for 24 h. The reaction mixture was cool to room temperature, and the solvent was removed by evaporation. The residues were washed with diethyl ether (20 mL) and dried to afford crude red solid. The crude product was then dissolved in water (20 mL), and NH_4PF_6 was added until no new precipitate was produced. The precipitate formed was washed with H_2O (50 mL), dried, and redissolved in acetone (20 mL). Saturated $(t\text{-Bu})_4$NCl was added dropwise until no new precipitate was produced. The precipitate that formed was washed with acetone (50 mL) and dried to afford **5**·2Cl (96 mg, 63%). ^{1}H NMR (400 MHz, D_2O): δ 8.88 (d, J = 6.8 Hz, 2H), 7.91 (d, J = 6.5 Hz, 3H), 7.63 (s, 2H), 7.52 (s, 5H), 7.42 (s, 2H), 5.81 (s, 3H), 2.61 (s, 4H), 1.47 (s, 3H). ^{13}C NMR (101 MHz, D_2O): δ 155.24, 151.17, 146.01, 143.75, 143.30, 133.37, 132.88, 132.06, 129.90, 129.83, 129.58, 128.94, 128.67, 128.36, 127.52, 63.97, 12.84, 12.53. HRMS (ESI): calcd for $C_{43}H_{39}N_4BF_2$ $[M-2Cl]^{2+}$: 330.1613; found, 330.1619.

Crystal. The single crystal of $\mathbf{BBox}^{4+}$ was obtained by the slow evaporation of diisopropyl ether into the acetonitrile solution of **BBox**·4PF_6 at room temperature for 7 days. Crystal data and the X-ray crystal structure with their CCDC numbers are provided in Table S4. CIF is available as a separate file as Supporting Information.

Preparation of Dox ⊂ BBox·4Cl and Dox ⊂ BBox·4Cl@HACD. **BBox**·4Cl (13.1 mg, 0.01 mmol) and doxorubicin (Dox) hydrochloride (5.8 mg, 0.01 mmol) were dissolved in distilled water (5 mL), and the solution was sonicated for 10 min. For Dox ⊂ **BBox**·4Cl@HACD, an additional HACD (75 mg, 0.015 mmol) were required to be added to the solution of Dox ⊂ **BBox**·4Cl. The obtained 2 mM Dox ⊂ **BBox**·4Cl or Dox ⊂ **BBox**·4Cl@HACD stock solution could be used directly for experiments or lyophilized as needed.

Detection of $^1O_2$ Production with ABDA. 9,10-Anthracenediyl-bis(methylene)dimalonic acid (ABDA) was employed as a specific $^1O_2$ probe to detect the generation of $^1O_2$ in solution (Scheme S1). When $^1O_2$ was generated after irradiation, ABDA could be oxidized with an increase in absorption at 375 nm. Specifically, 10 μM $\mathbf{BBox}^{4+}$ species or its reference compound **5**·2Cl containing 50 μM ABDA were placed in a cuvette and irradiated with a white light (λ > 420 nm, 220 mW/cm^2). The absorption band centered at 375 nm of the samples was then detected by the UV–vis spectroscopy. RB was used as a standard for evaluating the $^1O_2$ quantum yield of photosensitizers (Φ_{PS}), which could be calculated by the following equation[55]

$$\Phi_{PS} = \Phi_{RB}\frac{k_{PS}/k_{RB}}{A_{PS}/A_{RB}}$$

where k_{PS} and k_{RB} represent the decomposition rate constants of ABDA with photosensitizers (PS) and RB, respectively. A_{PS} and A_{RB} represent the integration areas of PS and RB under the absorption band in the wavelength range above 420 nm. Φ_{RB} is a known constant with a value of 75%.

Cyclic Voltammetry Measurement for 5·2PF_6 and BBox·4PF_6. Cyclic voltammogram experiments were conducted by using a three-electrode system. A glassy carbon electrode was used as the working electrode, and the platinum chip electrode and the Ag/AgCl electrode were used as the counter electrode and reference electrode, respectively. The measurement was conducted in acetonitrile containing 0.1 M tetrabutylammonium hexafluorophosphate with a scan rate of 200 mV/s.

Detection of the Dox Release from Nanoparticles. Dialysis bag (molecular weight cutoff: 1000 Da) containing Dox alone or Dox ⊂ **BBox**·4Cl@HACD (2 mL, 1 mM) solution was settled in the NaH_2PO_4/Na_2HPO_4 buffer solution (30 mL, pH = 7.4, 6.5, or 5.5) and dialyzed on a shaker at 37 °C. An aliquot (0.1 mL) was taken from the dialysate, and the absorption values (A_s) were read by a microplate reader at a wavelength of 480 nm. The percentage of Dox release was calculated by the following equation

https://doi.org/10.1021/acs.jmedchem.5c00094
J. Med. Chem. XXXX, XXX, XXX–XXX

$$\text{Dox release} = \frac{A_s - A_n}{A_p - A_n} \times 100\%$$

where A_s, A_n, and A_p represent the absorbances at 480 nm of the sample, positive control (complete release), and negative control (no release), respectively.

Identification of ROS with TMB in Solution. 3,3′,5,5′-Tetramethylbenzidine (TMB) was used to trap ROS in solution to generate oxidized TMB with a characteristic absorption at 652 nm (Scheme S2). To a 3.0 mL Dox ⊂ **BBox**·4Cl@HACD (10 μM) solution was added 80 μL of TMB stock solution (3.9 mM in DMSO). Different ROS quenchers, including L-tryptophan, D-mannitol, catalase, and superoxide dismutase (SOD), if needed, were subsequently added into the system ([L-tryptophan] = [D-mannitol] = 8 mM, [catalase] = [SOD] = 0.5 mg/mL). Samples were irradiated with a white light (λ > 420 nm, 220 mW/cm^2), and the absorption band centered at 652 nm was then detected by UV−vis spectroscopy.

Detection of $^1O_2$ and $^•$OH Production with EPR Spectroscopy. 2,2,6,6-Tetramethyl-4-piperidinone (TEMP) or 5,5-dimethyl-1-pyrroline *N*-oxide (DMPO) as spin-trap agents were employed to confirm the generation of $^1O_2$ and $^•$OH, respectively. EPR signals of the following six groups were collected: (1) TMEP (0.3 M) or DMPO (45 mM) with white light irradiation (λ > 420 nm, 220 mW/cm^2); (2) **BBox**·4Cl (0.1 mM) containing TMEP (0.3 M) or DMPO (45 mM) with white light irradiation (λ > 420 nm, 220 mW/cm^2); (3) Dox ⊂ **BBox**·4Cl (0.1 mM) containing TMEP (0.3 M) or DMPO (45 mM) with white light irradiation (λ > 420 nm, 220 mW/cm^2); (4) Dox ⊂ **BBox**·4Cl@HACD (0.1 mM) containing TMEP (0.3 M) or DMPO (45 mM) without irradiation; (5) Dox ⊂ **BBox**·4Cl@HACD (0.1 mM) containing TMEP (0.3 M) or DMPO (45 mM) with a white light irradiation (λ > 420 nm, 220 mW/cm^2). (6) The mixture of TEMP (0.3 M) or DMPO (45 mM), Dox (0.1 mM), and HACD (0.15 mM) with a white light irradiation (λ > 420 nm, 220 mW/cm^2).

Photocurrent Measurement. A CS310H electrochemical workstation with a standard three-electrode system was used for photoelectrochemical measurements. Five mg of photosensitizer was dispersed in a mixed solution (10 μL of 5% Nafion and 2 mL of ethanol) with ultrasound. Then, 100 μL suspension was dropped onto the ITO plate with 1 cm^2 and dried to be the working electrode. The counter electrode and the reference electrode were a Pt plate and Ag/AgCl. The electrolyte was a 0.1 M Na_2SO_4 solution. The photocurrent test and photovoltage were measured under a 300 W Xe lamp with an interval of 30 s.

Flow Cytometry. A549 cells were seeded onto six-well plates and incubated in F12 medium containing 10% FBS and 1% penicillin−streptomycin solution for 12 h until the cell density reached 1 × 10^6. Fresh F12 medium containing Dox ⊂ **BBox**·4Cl@HACD (2 μM, 2 mL) was replaced and incubated for different time intervals (6, 12, 18, and 24 h). Negative control (0 h) was only replaced with blank fresh F12 medium without drug. Cells were washed three times with PBS, digested with trypsin, centrifuged at 900 r for 2 min, dispersed with 2 mL PBS, and measured by Mindray BriCyte E6. The excitation filter was 488 nm, and the signals of the green channel were received.

Detection of ROS in Living Cells. The ROS assay kit was employed to detect the ROS in living cells. 2,7- Dichlorodihydrofluorescein diacetate (DCFH-DA) can freely cross the cell membrane and be hydrolyzed by esterase to DCFH, which cannot cross the cell membrane, and the latter can be oxidized by ROS to green fluorescence emissive DCF. Specifically, A549 cells and 293T cells were incubated at 37 °C for 12 h in F12 or DMEM medium containing 10% FBS and 1% penicillin−streptomycin solution. After incubated with Dox ⊂ **BBox**·4Cl@HACD (0.5 μM) for another 12 h, the cells were washed twice with filtered PBS, replaced the medium containing DCFH-DA (10 μM), and incubated for 20 min to let DCFH-DA cross the membrane. After washing twice with 1× PBS and replacing with normal medium, cells were irradiated with a white light (λ > 420 nm, 220 mW/cm^2) for 10 min, and then the medium was replaced with PBS. The green fluorescence was observed by LSCM with a 488 nm laser.

Detection NADH Consumption In Vitro. The NAD$^+$/NADH assay kit with WST-8 was used for monitoring NADH in A549 cells treated with different concentrations of Dox ⊂ **BBox**·4Cl@HACD. A549 cells were seeded on six-well plates and incubated for 24 h to ensure that the cell count reached 10^6. Fresh F12 medium containing different concentrations of Dox ⊂ **BBox**·4Cl@HACD was replaced and incubated for 12 h. Then, the cells were irradiated with a white light (λ > 420 nm, 220 mW/cm^2) for 10 min if needed, and the concentration of NADH was measured by the NAD$^+$/NADH assay kit.

Tumor Cells Inhibition In Vitro. A549 cells were seeded onto 96-well plates at a density of 5000 and incubated in F12 medium containing 10% FBS and 1% penicillin−streptomycin solution for 12 h under normoxic (21% O_2) and hypoxic (1.1% O_2) conditions, respectively. A fresh F12 medium containing various concentrations of drugs administrated was added to replace the previous medium, and cells were incubated for another 12 h. Then, cells were irradiated by a white light (λ > 420 nm, 220 mW/cm^2) for 10 min and incubated for 2 h. The cell growth was examined with a CCK-8 assay kit. The IC_{50} was calculated by the software IBM SPSS Statistic 26 and the combination index (CI) between drug A and drug B was calculated by the following equation[56]

$$CI = \frac{IC_{50}[A]}{IC_{50}A} + \frac{IC_{50}[B]}{IC_{50}B}$$

where $IC_{50}[A]$ and $IC_{50}[B]$ represent the concentrations of drug A and drug B, respectively, at which 50% inhibition is achieved when drug A and drug B are combined. $IC_{50}A$ and $IC_{50}B$ represent the concentrations at which drug A and drug B alone achieve 50% inhibition, respectively. According to Soriano's judgment method,[57] $0.9 \le CI \le 1.1$ is superposition, $0.8 \le CI < 0.9$ is low synergism, $0.6 \le CI < 0.8$ is moderate synergism, $0.4 \le CI < 0.6$ is high synergism, and $0.2 \le CI < 0.4$ is strong synergism.

Organelle Colocalization. A549 cells were seeded onto a laser confocal Petri dish and incubated for 12 h. Then, fresh F12 medium containing Dox ⊂ **BBox**·4Cl@HACD (2 μM) was added to the dish and incubated for another 12 h. Cells were irradiated by white light (λ > 420 nm, 220 mW/cm^2) for 10 min if needed. Subsequently, Mito-Tracker Red CMXRos, Lysotracker Red, and Hoechst33342 were added to stain the mitochondria, lysosome, and nucleus, as required at 37 °C, respectively. Cells were then washed with PBS and observed by the LSCM. For Mito-Tracker Red CMXRos and Lysotracker Red, the excitation filter was 559 nm, and the emission was 600−700 nm; for Dox ⊂ **BBox**·4Cl@HACD, the excitation filter was 488 nm, and the emission was 510−550 nm; For Hoechst 33342, the excitation filter was 405 nm, and the emission was 420−450 nm.

Detection of the Mitochondrial Membrane Potential. A549 cells were seeded onto a laser confocal Petri dish and incubated for 12 h. Then, fresh F12 medium containing Dox ⊂ **BBox**·4Cl@HACD (0.5 μM) was replaced and incubated for another 12 h. Cells were irradiated by a white light (λ > 420 nm, 220 mW/cm^2) for 10 min if needed. JC-1 was sonicated in buffer for 5 min and mixed with fresh F12 medium 1:1 by volume. The obtained JC-1 working fluid was added to stain cells for 20 min. Cells were then washed with buffer and measured by LSCM immediately.

Detection of Mitochondrial Permeability Transition. A549 cells were seeded onto a laser confocal Petri dish and incubated for 12 h. Then, fresh F12 medium containing Dox ⊂ **BBox**·4Cl@HACD (0.5 μM) was replaced and incubated for another 12 h. Cells were irradiated by a white light (λ > 420 nm, 220 mW/cm^2) for 10 min if needed. Fresh serum-free F12 medium containing calcein acetoxymethyl ester (calcein AM) was added, and the mixture was incubated for 30 min. Fresh F12 medium was replaced and incubated for another 30 min to ensure the formation of green-fluorescent calcein by hydrolysis. Fresh F12 medium containing $CoCl_2$ was replaced and incubated for 20 min if needed. Cells were then washed with PBS and observed by LSCM immediately.

https://doi.org/10.1021/acs.jmedchem.5c00094
J. Med. Chem. XXXX, XXX, XXX−XXX

Tumor Inhibition In Vivo. 4 week old BALB/c nude mice were obtained from Beijing FHK Bioscience Co. Ltd. The A549 tumor model was generated by subcutaneous inoculation on the armpit of mice (1×10^7 A549 cells in PBS, 100 μL). After 6 days after tumor implantation, the mice were randomly divided into six groups (four mice per group) for different treatment: (1) PBS (100 μL), (2) Dox (1.7 mM, 100 μL), (3) **BBox**·4Cl (1.7 mM, 100 μL) with white light irradiation (λ > 420 nm, 220 mW/cm^2), (4) Dox ⊂ **BBox**·4Cl (1.7 mM, 100 μL) with white light irradiation (λ > 420 nm, 220 mW/cm^2), (5) Dox ⊂ **BBox**·4Cl @HACD (1.7 mM, 100 μL) without irradiation, and (6) Dox ⊂ **BBox**·4Cl@HACD (1.7 mM, 100 μL) with white light irradiation (λ > 420 nm, 220 mW/cm^2). Mice in six groups were intravenously injected with drugs administrated, and irradiated with white light (λ > 420 nm, 220 mW/cm^2) for 600 s the next day if needed. The tumor volume and body weight of the mice were monitored for 14 days. The method for tumor volume (V) calculation was by the following equation

$$V = L_{\text{length}} \times L_{\text{width}}^2/2$$

After 14 days, mice were sacrificed, and the Tumor Growth Inhibition (TGI) value was calculated according to the following equation

$$\text{TGI} = (G_0 - G_T)/G_0$$

where G_0 and G_T represent the weight of the tumor in the PBS group and treatment groups, respectively.

Hemolysis Assay. 2% rabbit RBC in Alserver's solution were centrifuged at 3000 rpm for 10 min and washed with saline until the Alserver's solution was clear. Saline then was added to the erythrocyte pellets to achieve the final concentration of 5%. A series of 700 μL samples were made by mixing 5% RBC (140 μL) and saline (490 μL) with escalating concentrations of Dox ⊂ **BBox**·4Cl@HACD (70 μL) in saline. Different concentrations made by the halved dilution method with the concentration of Dox ⊂ **BBox**·4Cl@HACD to be from 0 to 64 μM were incubated for one h under 37 °C. After that, all the tubes were centrifuged at 3000 rpm for 10 min, and then the 100 μL supernatant was transferred to the 96-well plate to estimate the free hemoglobin at 570 nm by the microplate reader. Saline and deionized water were treated as the negative and positive controls, respectively. The hemolysis ratio was calculated by the following equation[58]

$$\text{hemolysis ratio} = \frac{A_s - A_n}{A_p - A_n} \times 100\%$$

where A_s, A_n, and A_p represent the absorbances at 570 nm of the testing sample and positive and negative controls, respectively.

Activated Partial Thromboplastin Time Assay. The samples consisted of different concentrations of Dox ⊂ **BBox**·4Cl@HACD (20 μL) and rabbit plasma (180 μL), which were incubated at 37 °C for 1 min. Subsequently, 200 μL of preheated aPTT reagent was added and incubated for another 2 min. Finally, 200 μL of 0.025 mol/L preheated $CaCl_2$ solution was added, and the clotting time was recorded.

Blood Urea Nitrogen and Creatinine Assays. BALB/c nude mice were intravenously injected with PBS (100 μL) or Dox ⊂ **BBox**·4Cl @HACD (1.7 mM, 100 μL) and incubated for 24 h. Mice were sacrificed, and the blood was collected from the heart, mixed with sodium citrate (109 mM) at a ratio of 9:1, and centrifuged at 3000 rpm for 10 min. The concentrations of blood urea nitrogen and creatinine of fresh extracted plasma were evaluated by blood urea nitrogen and creatinine assay kits, respectively.

Statistical Analysis. Statistical analysis of the data was carried out by an unpaired two-tailed t-test (IBM SPSS Statistics 22 software), and results were presented as either means ± SD or means ± SEM. P values ≤ 0.05 were considered significant, *p < 0.05, ***p < 0.001, ****p < 0.0001, and ns represents "no significant difference".

■ ASSOCIATED CONTENT

Supporting Information

The Supporting Information is available free of charge at https://pubs.acs.org/doi/10.1021/acs.jmedchem.5c00094.

^{1}H NMR, ^{13}C NMR, and HRMS spectra of all target compounds; fluorescence excitation and emission spectra; quantum yield; concentration-dependent and host−guest ^{1}H NMR spectra; Job's plot experiments; UV−vis and fluorescence titration; data of TEM and zeta potentials; data of ABDA photodegradation, TMB oxidation, and NADH depletion; profiles of flow cytometry and Pearson correlation coefficient; cell viability; HPLC trace; principles of the experiments of ABDA photodegradation and TMB oxidation; $^1O_2$ quantum yield of the compounds; the table of the comparison with BODIPY-based photosensitizers; and crystal data (PDF)

X-ray crystal structures of **BBox**$^{4+}$ (CCDC number: 2367093) have been deposited in the Cambridge Crystallographic Data Centre. Authors will release the atomic coordinates upon article publication (CIF)

Molecular formula strings (CSV)

■ AUTHOR INFORMATION

Corresponding Author

Yu Liu − *College of Chemistry, State Key Laboratory of Elemento-Organic Chemistry, Nankai University, Tianjin 300071, P. R. China;* orcid.org/0000-0001-8723-1896; Email: yuliu@nankai.edu.cn

Authors

Zhuo Lei − *College of Chemistry, State Key Laboratory of Elemento-Organic Chemistry, Nankai University, Tianjin 300071, P. R. China;* orcid.org/0000-0001-6042-6810

Ya-Hui Song − *College of Chemistry, State Key Laboratory of Elemento-Organic Chemistry, Nankai University, Tianjin 300071, P. R. China*

Yuan-Li Leng − *College of Chemistry, State Key Laboratory of Elemento-Organic Chemistry, Nankai University, Tianjin 300071, P. R. China*

Yi-Jun Gu − *Key Laboratory of Molecular Microbiology and Technology, College of Life Sciences, Nankai University, Tianjin 300071, China*

Miao Yu − *College of Chemistry, State Key Laboratory of Elemento-Organic Chemistry, Nankai University, Tianjin 300071, P. R. China*

Yong Chen − *College of Chemistry, State Key Laboratory of Elemento-Organic Chemistry, Nankai University, Tianjin 300071, P. R. China*

Qilin Yu − *Key Laboratory of Molecular Microbiology and Technology, College of Life Sciences, Nankai University, Tianjin 300071, China;* orcid.org/0000-0003-0473-5111

Complete contact information is available at: https://pubs.acs.org/10.1021/acs.jmedchem.5c00094

Author Contributions

The manuscript was written through the contributions of all authors. All authors have given approval to the final version of the manuscript.

Notes

The authors declare no competing financial interest.

https://doi.org/10.1021/acs.jmedchem.5c00094
J. Med. Chem. XXXX, XXX, XXX−XXX

■ ACKNOWLEDGMENTS

This work was financially supported by the National Natural Science Foundation of China (grants 22131008) and the Fundamental Research Funds for the Central Universities, Nankai University.

■ ABBREVIATIONS USED

NADH, nicotinamide adenine dinucleotide; BODIPY, boron dipyrromethene; PDT, photodynamic therapy; Dox, doxorubicin; HACD, β-cyclodextrin grafted-hyaluronic acid; SPR, supramolecular photoelectron "reservoir"; ROS, reactive oxygen species; MTX, methotrexate; ABDA, 9,10-Anthracenediyl-bis(methylene)dimalonic acid; CD44, cluster determinant 44; RHAMM, HA-mediated motility receptor; TEM, transmission electron microscopy; FE-SEM, field emission scanning electron microscope; DLS, dynamic light scattering; TMB, 3,3,5′,5′-tetramethylbenzidine; EPR, electron paramagnetic resonance; TEMP, 2,2,6,6-tetramethyl-4-piperidinone; DMPO, 5,5-dimethyl-1-pyrroline *N*-oxide; DCFH-DA, 6-carboxyl-2′,7′-dichlorodihydrofluorescein diacetate; MPTP, mitochondrial permeability transition pore; IC50, half-maximal inhibitory concentration; CI, combination index; TGI, tumor growth inhibition; H&E, hematoxylin and eosin; aPTT, activated partial thromboplastin time; HPLC, high-performance liquid chromatography

■ REFERENCES

(1) Schmidt, B. V. K. J.; Barner-Kowollik, C. Dynamic macromolecular material design—the versatility of cyclodextrin-based host–guest chemistry. *Angew. Chem., Int. Ed.* **2017**, *56*, 8350–8369.
(2) Liu, Z.; Liu, Y. Multicharged cyclodextrin supramolecular assemblies. *Chem. Soc. Rev.* **2022**, *51*, 4786–4827.
(3) Harada, A.; Takashima, Y.; Nakahata, M. Supramolecular polymeric materials via cyclodextrin–guest interactions. *Acc. Chem. Res.* **2014**, *47*, 2128–2140.
(4) Hanayama, H.; Yamada, J.; Tomotsuka, I.; Harano, K.; Nakamura, E. Rim binding of cyclodextrins in size-sensitive guest recognition. *J. Am. Chem. Soc.* **2021**, *143*, 5786–5792.
(5) Barrow, S. J.; Kasera, S.; Rowland, M. J.; del Barrio, J.; Scherman, O. A. Cucurbituril-based molecular recognition. *Chem. Rev.* **2015**, *115*, 12320–12406.
(6) Isaacs, L. Stimuli responsive systems constructed using cucurbit[n]uril-type molecular containers. *Acc. Chem. Res.* **2014**, *47*, 2052–2062.
(7) Yang, D.; Liu, M.; Xiao, X.; Tao, Z.; Redshaw, C. Polymeric self-assembled cucurbit[n]urils: synthesis, structures and applications. *Coord. Chem. Rev.* **2021**, *434*, 213733.
(8) Nimse, S. B.; Kim, T. Biological applications of functionalized calixarenes. *Chem. Soc. Rev.* **2013**, *42*, 366–386.
(9) Li, P.; Chen, Y.; Liu, Y. Calixarene/pillararene-based supramolecular selective binding and molecular assembly. *Chin. Chem. Lett.* **2019**, *30*, 1190–1197.
(10) Xue, M.; Yang, Y.; Chi, X.; Zhang, Z.; Huang, F. Pillararenes, a new class of macrocycles for supramolecular chemistry. *Acc. Chem. Res.* **2012**, *45*, 1294–1308.
(11) Zhang, H.; Liu, Z.; Zhao, Y. Pillararene-based self-assembled amphiphiles. *Chem. Soc. Rev.* **2018**, *47*, 5491–5528.
(12) Uekama, K.; Hirayama, F.; Irie, T. Cyclodextrin drug carrier systems. *Chem. Rev.* **1998**, *98*, 2045–2076.
(13) Webber, M. J.; Langer, R. Drug delivery by supramolecular design. *Chem. Soc. Rev.* **2017**, *46*, 6600–6620.
(14) Li, X.; Shen, M.; Yang, J.; Liu, L.; Yang, Y. W. Pillararene-based stimuli-responsive supramolecular delivery systems for cancer therapy. *Adv. Mater.* **2024**, *36*, 2313317.
(15) Qutub, S. S.; Bhat, I. A.; Maatouk, B. I.; Moosa, B.; Fakim, A.; Nawaz, K.; Diaz-Galicia, E.; Lin, W.; Grünberg, R.; Arold, S. T.; Khashab, N. M. An amphiphilic cell-penetrating macrocycle for efficient cytosolic delivery of proteins, DNA, and CRISPR Cas9. *Angew. Chem., Int. Ed.* **2024**, *63*, No. e202403647.
(16) Li, S.; Wang, Y.; Wang, X.; Feng, J.; Guo, D. S.; Meng, Z.; Liu, Y.; Sun, S. K.; Zhang, Z. Macrocyclic-albumin conjugates for precise delivery of radionuclides and anticancer drugs to tumors. *ACS Nano* **2023**, *17*, 22399–22409.
(17) Blanco-Gómez, A.; Cortón, P.; Barravecchia, L.; Neira, I.; Pazos, E.; Peinador, C.; García, M. D. Controlled binding of organic guests by stimuli-responsive macrocycles. *Chem. Soc. Rev.* **2020**, *49*, 3834–3862.
(18) Zhang, H.; Xu, W.; Li, G.; Qu, H.; Ma, C.; Noruzi, E. B.; He, Q.; Cheng, J.; Li, H. Controlled release system of nanopesticides based on noncovalent interactions. *ACS Agric. Sci. Technol.* **2024**, *4*, 851–871.
(19) Song, Y. H.; Bian, Q.; Wang, F.; Liu, J.; Yang, Y. H.; Zhang, Y. M.; Liu, Y. Water-soluble stimuli-responsive supramolecular nanoagrochemicals based on macrocycle compounds. *Coord. Chem. Rev.* **2025**, *524*, 216299.
(20) Lai, W. F.; Rogach, A. L.; Wong, W. T. Chemistry and engineering of cyclodextrins for molecular imaging. *Chem. Soc. Rev.* **2017**, *46*, 6379–6419.
(21) Zhou, W. L.; Lin, W.; Chen, Y.; Liu, Y. Supramolecular assembly confined purely organic room temperature phosphorescence and its biological imaging. *Chem. Sci.* **2022**, *13*, 7976–7989.
(22) Wu, Q.; Zhou, Z.; Xu, L.; Zhong, H.; Xiong, B.; Ren, T.; Li, Z.; Yuan, L.; Zhang, X. B. Multivalent supramolecular fluorescent probes for accurate disease imaging. *Sci. Adv.* **2024**, *10*, No. eadp8719.
(23) Jiao, J. B.; Wang, G. Z.; Hu, X. L.; Zang, Y.; Maisonneuve, S.; Sedgwick, A. C.; Sessler, J. L.; Xie, J.; Li, J.; He, X. P.; Tian, H. Cyclodextrin-based peptide self-assemblies (Spds) that enhance peptide-based fluorescence imaging and antimicrobial effcacy. *J. Am. Chem. Soc.* **2020**, *142*, 1925–1932.
(24) Li, X.; Lee, S.; Yoon, J. Supramolecular photosensitizers rejuvenate photodynamic therapy. *Chem. Soc. Rev.* **2018**, *47*, 1174–1188.
(25) Min, X.; Yi, F.; Han, X. L.; Li, M.; Gao, Q.; Liang, X.; Chen, Z.; Sun, Y.; Liu, Y. Targeted photodynamic therapy using a water-soluble aggregation-induced emission photosensitizer activated by an acidic tumor microenvironment. *Chem. Eng. J.* **2022**, *432*, 134327.
(26) Huang, Q.; Ding, C.; Wang, W.; Yang, L.; Wu, Y.; Zeng, W.; Li, Z.; Shi, Z.; Mei, L.; Zeng, X.; Zhao, Y.; Chen, H. An "AND" logic gate–based supramolecular therapeuticnanoplatform for combatting drug-resistant non–smallcell lung cancer. *Sci. Adv.* **2024**, *10*, No. eadp9071.
(27) Li, Q. L.; Sun, Y.; Ren, L.; Wang, X.; Wang, C.; Li, L.; Yang, Y. W.; Yu, X.; Yu, J. Supramolecular nanosystem based on pillararene-capped CuS nanoparticles for targeted chemo-photothermal therapy. *ACS Appl. Mater. Interfaces* **2018**, *10*, 29314–29324.
(28) Yang, J.; Dai, D.; Lou, X.; Ma, L.; Wang, B.; Yang, Y. W. Supramolecular nanomaterials based on hollow mesoporous drug carriers and macrocycle-capped CuS nanogates for synergistic chemo-photothermal therapy. *Theranostics* **2020**, *10*, 615–629.
(29) Gao, J.; Yu, H. M.; Wu, M.; Chen, Q.; Yang, Y.; Qu, Y.; Sun, M.; Qin, J. C.; Ma, L.; Yang, Y. W. AuNRs@MIL-101-based stimuli-responsive nanoplatform with supramolecular gates for image-guided chemo-photothermal therapy. *Mater. Today. Chem.* **2022**, *23*, 100716.
(30) Zhou, J.; Gu, J.; Sun, X.; Ye, Q.; Wu, X.; Xi, J.; Han, J.; Liu, Y. supramolecular chiral binding affinity-achieved efficient synergistic cancer therapy. *Adv. Sci.* **2024**, *11*, 2308493.
(31) Kwon, N.; Kim, H.; Li, X.; Yoon, J. Supramolecular agents for combination of photodynamic therapy and other treatments. *Chem. Sci.* **2021**, *12*, 7248–7268.
(32) Liu, K.; Liu, Y.; Yao, Y.; Yuan, H.; Wang, S.; Wang, Z.; Zhang, X. Supramolecular photosensitizers with enhanced antibacterial efficiency. *Angew. Chem., Int. Ed.* **2013**, *52*, 8285–8289.
(33) Gao, Z.; Zheng, X.; Dong, X.; Liu, W.; Sha, J.; Bian, S.; Li, J.; Cong, H.; Lee, C. S.; Wang, P. A general strategy for enhanced photodynamic antimicrobial therapy with perylenequinonoid photo-

https://doi.org/10.1021/acs.jmedchem.5c00094
J. Med. Chem. XXXX, XXX, XXX–XXX

sensitizers using a macrocyclic supramolecular carrier. *Adv. Healthcare Mater.* **2024**, *13*, 2401778.
(34) Roy, I.; Bobbala, S.; Young, R. M.; Beldjoudi, Y.; Nguyen, M. T.; Cetin, M. M.; Cooper, J. A.; Allen, S.; Anamimoghadam, O.; Scott, E. A.; Wasielewski, M. R.; Stoddart, J. F. A supramolecular approach for modulated photoprotection, lysosomal delivery, and photodynamic activity of a photosensitizer. *J. Am. Chem. Soc.* **2019**, *141*, 12296−12304.
(35) Ikeda, A.; Satake, S.; Mae, T.; Ueda, M.; Sugikawa, K.; Shigeto, H.; Funabashi, H.; Kuroda, A. Photodynamic activities of porphyrin derivative−cyclodextrin complexes by photoirradiation. *ACS Med. Chem. Lett.* **2017**, *8*, 555−559.
(36) Yuan, B.; Wu, H.; Wang, H.; Tang, B.; Xu, J. F.; Zhang, X. A self-degradable supramolecular photosensitizer with high photodynamic therapeutic efficiency and improved safety. *Angew. Chem., Int. Ed.* **2021**, *60*, 706−710.
(37) Tang, M.; Liu, Y. H.; Liu, H.; Mao, Q.; Yu, Q.; Kitagishi, H.; Zhang, Y. M.; Xiao, L.; Liu, Y. Supramolecular dual polypeptides induced tubulin aggregation for synergistic cancer theranostics. *J. Med. Chem.* **2022**, *65*, 13473−13481.
(38) Teng, K. X.; Niu, L. Y.; Yang, Q. Z. A host−guest strategy for converting the photodynamic agents from a singlet oxygen generator to a superoxide radical generator. *Chem. Sci.* **2022**, *13*, 5951−5956.
(39) Zhang, Y.; Wang, Y.; Chen, T.; Han, Y.; Yan, C.; Wang, J.; Lu, B.; Ma, L.; Ding, Y.; Yao, Y. Pillar[5]arene based water-soluble [3]pseudorotaxane with enhanced fluorescence emission for cell imaging and both type and photodynamic cancer therapy. *Chem. Commun.* **2023**, *59*, 8266−8269.
(40) Deng, X.; Shao, Z.; Zhao, Y. Solutions to the drawbacks of photothermal and photodynamic cancer therapy. *Adv. Sci.* **2021**, *8*, 2002504.
(41) Wang, Y. Y.; Liu, Y. C.; Sun, H.; Guo, D. S. Type I photodynamic therapy by organic-inorganic hybrid materials: from strategies to applications. *Coord. Chem. Rev.* **2019**, *395*, 46−62.
(42) Wan, Y.; Fu, L. H.; Li, C.; Lin, J.; Huang, P. Conquering the hypoxia limitation for photodynamic therapy. *Adv. Mater.* **2021**, *33*, 2103978.
(43) Garci, A.; Abid, S.; David, A. H. G.; Jones, L. O.; Azad, C. S.; Ovalle, M.; Brown, P. J.; Stern, C. L.; Zhao, X.; Malaisrie, L.; Schatz, G. C.; Young, R. M.; Wasielewski, M. R.; Stoddart, J. F. Exciplex emission and förster resonance energy transfer in polycyclic aromatic hydrocarbon-based bischromophoric cyclophanes and homo[2]-catenanes. *J. Am. Chem. Soc.* **2023**, *145*, 18391−18401.
(44) He, Z.; Mei, L.; Connell, M.; Maxwell, C. A. Hyaluronan mediated motility receptor (HMMR) encodes an evolutionarily conserved homeostasis, mitosis, and meiosis regulator rather than a hyaluronan receptor. *Cells* **2020**, *9*, 819.
(45) Carvalho, A. M.; Soares, D. S. D.; Paulo, P. M. R.; Reis, R.; Pashkuleva, I. Co-localization and crosstalk between CD44 and RHAMM depend on hyaluronan presentation. *Acta Biomater.* **2021**, *119*, 114−124.
(46) Hamilton, S. R.; Fard, S. F.; Paiwand, F. F.; Tolg, C.; Veiseh, M.; Wang, C.; McCarthy, J. B.; Bissell, M. J.; Koropatnick, J.; Turley, E. A. The hyaluronan receptors CD44 and Rhamm (CD168) form complexes with ERK1,2 that sustain high basal motility in breast cancer cells. *J. Biol. Chem.* **2007**, *282*, 16667−16680.
(47) Jiao, Y.; Đorđević, L.; Mao, H.; Young, R. M.; Jaynes, T.; Chen, H.; Qiu, Y.; Cai, K.; Zhang, L.; Chen, X. Y.; Feng, Y.; Wasielewski, M. R.; Stupp, S. I.; Stoddart, J. F. A donor−acceptor [2]catenane for visible light photocatalysis. *J. Am. Chem. Soc.* **2021**, *143*, 8000−8010.
(48) Santidrian, A. F.; Matsuno-Yagi, A.; Ritland, M.; Seo, B. B.; LeBoeuf, S. E.; Gay, L. J.; Yagi, T.; Felding-Habermann, B. Mitochondrial complex I activity and NAD^+/NADH balance regulate breast cancer progression. *J. Clin. Invest.* **2013**, *123*, 1068−1081.
(49) Teng, K. X.; Zhang, D.; Liu, B. K.; Liu, Z. F.; Niu, L. Y.; Yang, Q. Z. Photo-induced disproportionation-mediated photodynamic therapy: simultaneous oxidation of tetrahydrobiopterin and generation of superoxide radicals. *Angew. Chem., Int. Ed.* **2024**, *63*, No. e202318783.
(50) He, R.; Zhang, Y.; Madhu, S.; Gao, Q.; Lian, Q.; Raghavan, S. S.; Geng, J. BODIPY based realtime, reversible and targeted fluorescent probes for biothiol imaging in living cells. *Chem. Commun.* **2020**, *56*, 14717−14720.
(51) Gupta, G.; Das, A.; Lee, J.; Mandal, N.; Lee, C. Y. Self-assembled BODIPY-based iridium metallarectangles: cytotoxicity and propensity to bind biomolecules. *ChemPlusChem* **2018**, *83*, 339−347.
(52) Gupta, G.; Das, A.; Park, K. C.; Tron, A.; Kim, H.; Mun, J.; Mandal, N.; Chi, K. W.; Lee, C. Y. Self-assembled novel BODIPY-based palladium supramolecules and their cellular localization. *Inorg. Chem.* **2017**, *56*, 4615−4621.
(53) Hassanain, H.; Davies, E. S.; Lewis, W.; Kays, D. L.; Champness, N. R. Structural characterization and optical properties of two copper(i)-iodide BODIPY coordination polymers. *CrystEngComm* **2019**, *21*, 4551−4556.
(54) Yang, Y.; Zhang, Y.-M.; Chen, Y.; Chen, J.-T.; Liu, Y. Targeted Polysaccharide Nanoparticle for Adamplatin Prodrug Delivery. *J. Med. Chem.* **2013**, *56*, 9725−9736.
(55) Dong, X.; Dai, X.; Li, G.; Zhang, Y. M.; Xu, X.; Liu, Y. Conformationally Confined Emissive Cationic Macrocycle with Photocontrolled Organelle-Specific Translocation. *Adv. Sci.* **2022**, *9*, 2201962.
(56) Chou, T. C. Drug Combination Studies and Their Synergy Quantification Using the Chou-Talalay Method. *Cancer Res.* **2010**, *70*, 440−446.
(57) Soriano, A. F.; Helfrich, B.; Chan, D. C.; Heasley, L. E.; Jr, P. A. B.; Chou, T. C. Synergistic Effects of New Chemopreventive Agents and Conventional Cytotoxic Agents against Human Lung Cancer Cell Lines. *Cancer Res.* **1999**, *59*, 6178−6184.
(58) Zong, Y.; Lei, Z.; Yu, S. B.; Zhang, L. Y.; Wu, Y.; Feng, K.; Qi, Q. Y.; Liu, Y.; Zhu, Y.; Guo, P.; Zhou, W.; Zhang, D. W.; Li, Z. T. Caltrop-like Small-Molecule Antidotes That Neutralize Unfractionated Heparin and Low-Molecular-Weight Heparin In Vivo. *J. Med. Chem.* **2024**, *67*, 3860−3873.

https://doi.org/10.1021/acs.jmedchem.5c00094
J. Med. Chem. XXXX, XXX, XXX−XXX